AgriEngineering

Article

Three-Dimensional Diffusion-Dominated Modeling of Coupled Heat and Moisture Transfer in Porous Grain Beds: A Low-Aeration Numerical Case Study

Normakhmad Ravshanov [1], Istam Shadmanov [2], Zukhro Adizova [2,*], Nodira Tashtemirova [1], Akbarali Izzatullayev [2], Zarina Murodova [3] and Aziza Zoirova [4]

[1] Laboratory of Modeling Complex Systems, Digital Technologies and Artificial Intelligence Research Institute, Tashkent 100125, Uzbekistan; nodira3110@mail.ru (N.T.)
[2] Department of Information Systems and Digital Technologies, Bukhara State University, Bukhara 200114, Uzbekistan; i.u.shadmanov@buxdu.uz (I.S.); a.e.izzatulloyev@buxdu.uz (A.I.)
[3] Department of Exact Sciences and Digital Technologies, Asian International University, Bukhara 200100, Uzbekistan; zarinamuradova212@gmail.com
[4] Department of Oil and Gas Processing Technology, Bukhara State Technical University, Bukhara 200117, Uzbekistan; aziza.z.1991@mail.ru
* Correspondence: z.m.adizova@buxdu.uz or zuhroadizova096@gmail.com

Abstract

Hidden self-heating and localized vapor accumulation are important mechanisms of quality deterioration during grain storage. A three-dimensional diffusion-dominated model is developed for coupled heat and moisture transfer in a porous grain bed under low aeration, solving temperature, grain moisture content and pore air absolute humidity with respiration heat generation, grain-air vapor exchange and Robin-type boundary exchange. For the baseline 1.0 m × 1.0 m × 0.5 m case, the 20 × 20 × 10 grid predicts at 28.3 h a peak temperature of 30.72 °C and a maximum pore air humidity of 15.79 g kg^{-1}, while grain moisture remains at 14.00% d.b., because the solid phase stores about 1.7 × 10^3 times more water per unit volume than the pore air. With a common time step, peak values differ by less than 0.01% between the base and fine grids; the peak temperature agrees with an analytical adiabatic-core solution to about 0.01 °C, and the water and energy balances close to machine precision. The reference respiration source dominates the thermal response (+12.79/−6.41 °C for ±50%), an asymmetry explained by the approach to finite-time thermal runaway, whereas the interphase vapor-transfer coefficient controls pore air humidity and interacts strongly with respiration. Non-uniform initial fields relocate and intensify the hot spot. A Darcy-Boussinesq check with the measured permeability of wheat leaves the temperature field unchanged (<0.01 °C) but lowers the maximum humidity by up to 10% and shifts it to the upper bed; a semi-implicit Crank-Nicolson scheme reproduces the explicit results with 15-fold larger time steps, and Sobol' indices confirm the dominance of the respiration parameters. The study is a reproducible numerical benchmark; no independent experimental validation is claimed.

Keywords: grain storage; porous grain bed; coupled heat and moisture transfer; respiration heat generation; numerical modeling

Academic Editor: Ray E. Sheriff

Received: 6 October 2026
Revised: 12 November 2026
Accepted: 18 November 2026
Published: 24 November 2026

Copyright: © 2026 by the authors. Licensee MDPI, Basel, Switzerland. This article is an open access article distributed under the terms and conditions of the Creative Commons Attribution (CC BY) license.

1. Introduction

The safe storage of cereal grains is governed by coupled heat and moisture processes inside a porous biological medium. Non-uniform porosity, packing density, ventilation and boundary exchange generate internal temperature and humidity gradients, so that local self-heating and moisture accumulation can develop before any visible deterioration or surface anomaly is observed [1,2]. Reliable assessment of storage risk therefore requires models that describe the simultaneous evolution of temperature, grain moisture content and pore air humidity.

Recent studies have emphasized the role of heterogeneous structure and ventilation. A mesoscale model of a wheat silo with non-uniform porosity reproduced measured temperature and moisture better than a uniform-porosity model [3]; pore-scale and computed-tomography-based models of barley and maize piles showed that local packing creates spatially heterogeneous transfer coefficients and strong gradients along the airflow direction [4,5]; and porous-medium models of corn piles and silos have been used to analyze coupled drying and the energy demand of different ventilation patterns [6,7]. Localized high-temperature, high-humidity regions and humidity-stratified layers in rice and paddy bulks have recently been studied as separate problems [8,9]. A grain bulk therefore cannot be treated as perfectly uniform when local hot spots and high-humidity zones are of interest.

Internal biological activity adds positive feedback. Respiration heat depends on temperature, moisture content and water activity, so that a moderate local warming intensifies metabolic heat release and can lead to self-heating [10–12]. Heat production of wet wheat measured under adiabatic conditions reaches about 0.10–0.15 W per kg of dry matter, and field hot spots rising by several degrees per day have been reported [13]. If heat removal through the boundaries is insufficient, hidden internal zones form that accelerate quality loss, microbial activity and condensation.

Storage models range from lumped energy–mass balances, which describe average trends but not localized hot spots [1,2], to spatially resolved diffusion, diffusion–advection and multiphase formulations in which heat, grain moisture and pore air vapor are solved as separate fields with convective (Robin-type) exchange at walls and headspace [14–18]. A key difficulty is the consistent representation of the respiration heat Q_r and of the interphase moisture exchange S_v, and the choice of the equilibrium closure that links the solid and gas phases: Chung–Pfost, Henderson-Thompson and GAB-type isotherms differ in temperature correction and hysteresis treatment, which affects predicted equilibration times and vapor-accumulation zones [19–24].

Experiments in instrumented columns and pilot silos show that the dominant transport mechanism depends on aeration intensity: diffusion-driven redistribution prevails at low aeration, whereas forced aeration can reverse gradients or displace hot spots [25–29]. Pore air humidity adjusts rapidly, temperature more slowly and grain moisture the slowest, because the effective grain-moisture diffusivity is much smaller than the thermal and vapor diffusivities [14,30]. Three-dimensional simulations of unventilated corn and wheat silos with natural convection and solar loading predict central or upper thermal cores and high relative humidity near the roof and walls [31,32]; in a comparative two-/three-dimensional study, the peak average temperatures differed by about 1 °C while the three-dimensional model required a much longer computing time [31], so that dimensionality is a trade-off between geometric fidelity and cost. The present formulation builds on the coordinate-splitting finite-difference framework developed by the authors' group for heat and moisture transfer in raw cotton and other porous products [33–37].

Explicit finite-difference schemes remain attractive because of their transparent structure and straightforward coupling between equations, provided that the stability constraint is satisfied [15,34]. Grid-refinement and conservation checks are nevertheless

https://doi.org/10.3390/agriengineering8120508

needed to ensure that predicted hot spots are not numerical artifacts, and diffusivities, boundary coefficients and source parameters are often correlated and poorly constrained [27–29]. At the same time, digital monitoring, for example, distributed optical-fiber temperature sensing combined with simulation and machine learning [38], increasingly requires physics-based interpretation of unobserved internal fields. Two limitations persist: many models do not jointly resolve T, M and W with a physically consistent interphase closure, and effective coefficients and empirical source terms are often introduced without clear links to measurable properties.

This study addresses these issues with a three-dimensional diffusion-dominated model of coupled heat and moisture redistribution in an effective porous grain bed under low-aeration conditions. Grain-air exchange is expressed through the water activity at the grain surface, the equilibrium interfacial humidity and a volumetric vapor-transfer term rather than by comparing M and W directly. The contributions are: (i) a coupled three-dimensional system for T, M and W; (ii) physically interpretable effective transport and source terms; (iii) a water-activity-based exchange closure; (iv) a conservative finite-difference discretization with Robin boundary fluxes; and (v) reproducible numerical verification (grid and time-step refinement, an analytical check of the respiration source and global water and energy balances) together with one-at-a-time, factorial and robustness analyses. The paper is a computational case study and does not claim calibration or independent experimental validation.

2. Materials and Methods

2.1. Problem Formulation

The present formulation is intended for low-aeration or weakly ventilated storage conditions in which diffusion and local source terms dominate the redistribution of heat and moisture within the grain bulk. Interstitial air motion, forced aeration and buoyancy-driven natural convection are not explicitly solved in the current version of the model. Therefore, the model should be interpreted as an idealized diffusion-dominated case study rather than as a complete general-purpose silo-scale aeration model.

This restriction is important because temperature and humidity gradients in real grain silos may induce air movement through the pore space. Under such conditions, heat and vapor transport by airflow, permeability of the grain bed and Darcy-type airflow should be included. In the present study, these mechanisms are not treated as physically unimportant in all storage systems; rather, they are excluded in order to isolate the coupled effects of effective diffusion, respiration heat generation, grain-air interphase vapor exchange and convective exchange at the external boundaries.

Accordingly, the conclusions of this study are limited to storage regimes where internal airflow is sufficiently weak and where the dominant transport mechanisms can be approximated by diffusion, local heat generation and boundary heat–mass exchange. Extension of the model to include Darcy airflow, natural convection and airflow-driven vapor transport is considered a necessary step for direct operational application to strongly ventilated or large-scale industrial silos. These statements describe the baseline model. A Darcy-Boussinesq airflow extension is formulated in Section 2.11 and applied in Section 3.12 to test the diffusion-dominated assumption for the present bed.

The grain bulk was considered as an effective porous medium occupying a bounded three-dimensional rectangular domain:

$$\Omega = (0, L_x) \times (0, L_y) \times (0, L_z) \subset \mathbb{R}^3,$$

where L_x, L_y and L_z denote the length, width and height of the storage region. The medium consists of two interacting phases: the solid grain phase and the intergranular air phase. The coupled thermodynamic state of the stored grain was described by three field

variables: temperature $T(x, y, z, t)$, grain moisture content $M(x, y, z, t)$ and pore air absolute humidity $W(x, y, z, t)$.

The purpose of the model is to describe heat and moisture redistribution in an effective porous grain bed under the combined action of internal and external processes. Internal processes include biological heat release caused by grain respiration, moisture exchange between grain kernels and pore air, and latent heat associated with phase interaction. External processes are represented by convective heat and pore air humidity exchange at the lateral and upper boundaries. The lower boundary is assumed insulated and impermeable.

2.2. Assumptions and Limitations

To clarify the scope within which the results of this study should be interpreted, the main assumptions underlying the model are stated explicitly below.

1. **Diffusion-dominated transport.** Interstitial airflow is assumed to be weak enough that advective (Darcy-type) transport and buoyancy-driven natural convection can be neglected in comparison with conductive heat diffusion and Fickian moisture/vapor diffusion. This restricts direct applicability to low-aeration or unventilated storage conditions; under forced aeration or strong natural convection, advective transport can dominate and displace the predicted hot-spot location [5,27–29,31]. This assumption is tested in Section 3.12 with a coupled Darcy-Boussinesq airflow model: for the present bed it holds for heat transfer but only approximately for pore air vapor transport.
2. **Effective-medium (continuum) representation.** The heterogeneous grain-air mixture is treated as an effective continuum with homogenized transport coefficients (λ_{eff}, D_M, D_W) obtained from porosity- and tortuosity-corrected mixing rules. Local kernel-to-kernel packing variability, grain orientation and non-uniform porosity fields are not resolved explicitly, unlike mesoscale pore-resolved models [3,4].
3. **Empirical, bounded source and closure terms.** The respiration source and the sorption relationship use empirical coefficients within the stated temperature and moisture range for the present numerical case. They are not proposed as universal biological or thermodynamic laws and should be re-estimated or calibrated when independent data for other grain types, moisture ranges or storage temperatures are available. In particular, the baseline respiration intensity represents a biologically active (hot-spot) scenario rather than sound grain at the stated moisture content (Section 2.7).
4. **No sorption hysteresis.** The grain-air equilibrium closure uses a single-valued sorption isotherm $f_s(T, M)$ and does not distinguish adsorption from desorption branches; hysteresis effects reported for cereal sorption isotherms [39] are therefore not captured. A bounding estimate of the resulting uncertainty is given in Sections 3.11 and 4.4.
5. **Spatially uniform initial state.** The baseline simulations start from spatially uniform initial fields T_0, M_0, W_0. Non-uniform initial conditions arising from filling history or prior storage can be incorporated in principle through sensor-based field reconstruction but were not considered here. Their effect on the position and magnitude of the hot spot is quantified in Section 3.11 and discussed in Section 4.2.
6. **Idealized rectangular geometry and boundary placement.** The domain is a rectangular parallelepiped with Robin exchange on the lateral and upper faces and a no-flux lower face. Cylindrical silo geometries, non-uniform wall exposure to solar radiation, and spatially varying boundary-transfer coefficients are not represented.
7. **Computational-only verification.** No independent experimental monitoring series is used in the present study. Numerical credibility is assessed through grid refinement, consistency of the conservative discretization, reproducible diagnostic outputs and one-at-a-time parameter sensitivity. Experimental calibration and field

validation remain future work. In the revised analysis, these checks are complemented by a fixed-time-step grid study, an analytical adiabatic-core solution, global water and energy balances, a factorial interaction analysis and robustness tests.

8. **Diagnostic, not operational, scope.** The model is intended as a physically interpretable diagnostic and benchmarking tool for storage-risk analysis. It is not proposed as a substitute for a full silo-scale operational control model, which would additionally require Darcy-type airflow, permeability-dependent transport, buoyancy coupling and field-scale multi-depth validation, as discussed further in the Discussion section.

2.3. Governing Equations

The coupled heat and moisture transfer process was represented by a system of three nonlinear parabolic balance equations. The heat equation is written in conservative form through the effective thermal conductivity λ_{eff}, and the corresponding thermal diffusivity is $D_T = \lambda_{eff}/(\rho c)$. The solid- and gas-phase moisture equations are also written as volumetric mass balances so that every term has units of $\mathrm{kg\,m^{-3}\,s^{-1}}$. The same interphase source $S_v(T, M, W)$ enters the two moisture balances with opposite signs:

$$\begin{cases} \rho c \dfrac{\partial T}{\partial t} = \nabla \cdot \left(\lambda_{eff} \nabla T\right) + Q_r(T, M) - L_v S_v(T, M, W), \\ \rho_s (1-\varepsilon) \dfrac{\partial M}{\partial t} = \nabla \cdot [\rho_s (1-\varepsilon) D_M \nabla M] - S_v(T, M, W), \\ \rho_a \varepsilon \dfrac{\partial W}{\partial t} = \nabla \cdot (\rho_a \varepsilon D_W \nabla W) + S_v(T, M, W). \end{cases} \quad (1)$$

Here, T is the grain-bed temperature, M is the grain moisture content on a dry basis, and W is the pore air absolute humidity ratio. The densities ρ_s and ρ_a and the phase-volume fractions $(1-\varepsilon)$ and ε convert the dimensionless moisture ratios into water mass per unit bulk volume. The corresponding diffusive mass fluxes are:

$$\mathbf{J}_M = -\rho_s (1-\varepsilon) D_M \nabla M, \qquad \mathbf{J}_W = -\rho_a \varepsilon D_W \nabla W,$$

with units of $\mathrm{kg\,m^{-2}\,s^{-1}}$. Consequently, their divergences and S_v all have units of $\mathrm{kg\,m^{-3}\,s^{-1}}$. This formulation keeps the diffusive fluxes dimensionally consistent with the volumetric interphase source.

The term $Q_r(T, M)$ describes respiration heat generation within the stored grain bulk. A positive S_v denotes evaporation from the grain phase into the pore air, whereas a negative S_v denotes condensation or vapor uptake by the grain. The latent-heat term $-L_v S_v$ therefore cools the bulk during evaporation and heats it during condensation. The opposite signs of S_v in the two moisture balances ensure internal conservation of water mass.

2.4. Estimation of Effective Thermal Diffusivity

The effective thermal diffusivity D_T was not introduced as an arbitrary fitting constant. It was calculated from the effective thermal conductivity and the volumetric heat capacity of the porous grain bulk as:

$$D_T = \frac{\lambda_{eff}}{\rho c}.$$

The effective thermal conductivity of the grain bed was estimated using a porosity-dependent geometric mixing rule:

$$\lambda_{eff} = \lambda_g^{1-\varepsilon} \lambda_a^{\varepsilon},$$

where λ_g is the thermal conductivity of the grain material, λ_a is the thermal conductivity of the pore air, and ε is the porosity of the grain bulk. This expression provides an effective-medium approximation for heat conduction through the combined solid-kernel and intergranular-air phases.

For wheat grain, the thermophysical parameters were selected within experimentally reported and literature-supported intervals [1,15,27,28]. The grain thermal conductivity was taken in the range:

$$0.17 \leq \lambda_g \leq 0.21 \text{ W m}^{-1} \text{ K}^{-1},$$

the thermal conductivity of air was taken as:

$$\lambda_a = 0.026 \text{ W m}^{-1} \text{ K}^{-1},$$

the bulk density was assumed within:

$$750 \leq \rho \leq 850 \text{ kg m}^{-3},$$

the effective specific heat capacity was selected as:

$$1800 \leq c \leq 2000 \text{ J kg}^{-1} \text{ K}^{-1},$$

and the porosity of the grain bulk was considered within:

$$0.38 \leq \varepsilon \leq 0.45.$$

Using representative values $\lambda_g = 0.19 \text{ W m}^{-1} \text{ K}^{-1}$, $\lambda_a = 0.026 \text{ W m}^{-1} \text{ K}^{-1}$, $\varepsilon = 0.40$, $\rho = 800 \text{ kg m}^{-3}$, and $c = 1900 \text{ J kg}^{-1} \text{ K}^{-1}$, the effective thermal conductivity becomes:

$$\lambda_{eff} = 0.19^{0.60} \cdot 0.026^{0.40} \approx 0.086 \text{ W m}^{-1} \text{ K}^{-1}.$$

Accordingly, the effective thermal diffusivity is:

$$D_T = \frac{0.086}{800 \cdot 1900} \approx 5.7 \times 10^{-8} \text{ m}^2 \text{ s}^{-1}.$$

Depending on bulk density, grain moisture state, packing structure and porosity, the calculated thermal diffusivity may vary within the order of 10^{-8}–10^{-7} m^2 s^{-1}. For the baseline computation, the representative value derived from the thermal-conductivity mixing rule and volumetric heat capacity was used directly; it was not fitted to an external monitoring series.

2.5. Estimation of Moisture and Vapor Diffusion Coefficients

The effective grain-moisture diffusivity D_M describes moisture migration within the solid grain phase. It was represented by:

$$D_M(T, M) = D_{M0} \exp\left[-\frac{E_M}{R}\left(\frac{1}{T_K} - \frac{1}{T_{0,K}}\right)\right][1 + \beta_M(M - M_0)],$$

where T_K and $T_{0,K}$ are absolute temperatures in kelvin, D_{M0} is the reference diffusivity, E_M is the activation energy, R is the universal gas constant and β_M is the moisture-sensitivity coefficient. The final values used in the calculations were $D_{M0} = 1.0 \times 10^{-9}$ m^2 s^{-1}, $E_M = 22$ kJ mol^{-1} and $\beta_M = 10$ (kg kg^{-1})$^{-1}$.

The effective pore air humidity diffusivity D_W represents the net vapor-redistribution rate in the unresolved intergranular pore network. The reference effective value was taken as:

$$D_W(T) = D_{W0}\left(\frac{T_K}{T_{0,K}}\right)^n, \qquad D_{W0} = 2.0 \times 10^{-8} \text{ m}^2 \text{ s}^{-1}, \quad n = 1.8.$$

This coefficient is an effective case-specific transport parameter rather than the free-air molecular diffusivity. Its lower magnitude accounts collectively for unresolved

tortuosity, pore constrictivity, stagnant pore regions and grain-air sorption buffering in the diffusion-dominated continuum representation.

Because D_{W0} is the least constrained transport coefficient, its influence was examined explicitly (Section 3.10). For reference, the tortuosity-corrected molecular diffusivity of water vapor in the pore air is about 6.7×10^{-6} m^2 s^{-1} (free-air value 2.5×10^{-5} m^2 s^{-1}, porosity 0.40, tortuosity 1.5), whereas the sorption-buffered effective moisture diffusivity of a grain bulk, in which the vapor flux is retarded by uptake on the kernels, is several orders of magnitude smaller [14]. The baseline value lies between these limits; increasing it by a factor of 335, up to the molecular limit, lowers the maximum pore air humidity from 15.79 to 13.49 g kg^{-1} but changes the peak temperature by less than 0.01 °C and does not move the humidity maximum (Section 3.10).

The interphase vapor-transfer coefficient in $S_v = K_v[W_i(T, M) - W]$ was treated separately from D_M and D_W. Because S_v has units of kg m^{-3} s^{-1} and $W_i - W$ is dimensionless, K_v has units of kg m^{-3} s^{-1}. It was decomposed as $K_v = \rho_a \beta_v$, where β_v is a specific volumetric exchange rate with units of s^{-1}.

The baseline $\beta_v = 2.0 \times 10^{-5}$ s^{-1} corresponds to a gas-phase relaxation time $\tau_v = \rho_a \varepsilon / K_v = 2.0 \times 10^4$ s ≈ 5.6 h, i.e., the time over which the pore air approaches the local interfacial equilibrium. No direct measurement of this coefficient for wheat was available; it is therefore treated as a case-specific parameter, varied in the sensitivity analysis (Sections 3.10 and 3.11) and identified in Section 4.6 as a priority for calibration.

2.6. Parameter Sources and Baseline Parameterization

The parameter set was assembled from literature-supported material properties, derived effective quantities and explicitly prescribed case-specific baseline coefficients. The initial and ambient state variables (T_0, M_0, W_0, T_∞ and W_∞), atmospheric pressure, domain dimensions and bulk density were prescribed for the numerical case. Material quantities such as grain and air thermal conductivity, heat capacity, porosity, grain-moisture diffusivity parameters, latent heat and GAB sorption parameters were selected within the admissible intervals summarized in Table 1. The reference pore air humidity diffusivity and exchange/source coefficients are treated as case-specific effective parameters and are examined by sensitivity analysis rather than fitted to observations.

Table 1. Complete model parameter set, admissible ranges and baseline simulation values.

Parameter	Symbol	Admissible Range	Baseline Value	Unit
Bulk grain density	ρ	750–850	800	kg m^{-3}
Solid grain density	ρ_s	1210–1390	1330	kg m^{-3}
Pore air density	ρ_a	1.15–1.25	1.20	kg m^{-3}
Specific heat capacity	c	1800–2000	1900	J kg^{-1} K^{-1}
Porosity	ε	0.38–0.45	0.40	–
Grain thermal conductivity	λ_g	0.17–0.21	0.19	W m^{-1} K^{-1}
Air thermal conductivity	λ_a	fixed	0.026	W m^{-1} K^{-1}
Effective thermal conductivity	λ_{eff}	derived	0.086	W m^{-1} K^{-1}
Thermal diffusivity	D_T	derived	5.7×10^{-8}	m^2 s^{-1}
Reference grain diffusivity	D_{M0}	1×10^{-10}–2×10^{-9}	1.0×10^{-9}	m^2 s^{-1}
Activation energy	E_M	15–30	22	kJ mol^{-1}
Moisture sensitivity	β_M	0–20	10	(kg kg^{-1})$^{-1}$
Temperature exponent	n	1.75–2.00	1.80	–
Pore air humidity diffusivity	D_{W0}	case-specific (Section 2.5)	2.0×10^{-8}	m^2 s^{-1}

Latent heat	L_v	$(2.40–2.50) \times 10^6$	2.45×10^6	J kg^{-1}
Boundary heat transfer	h_T	1.0–10.0	4.0	W m^{-2} K^{-1}
Boundary vapor transfer	h_W	2×10^{-6}–5×10^{-5}	1.2×10^{-5}	m s^{-1}
Volumetric vapor transfer	K_v	0.6×10^{-5}–8×10^{-5}	2.4×10^{-5}	kg m^{-3} s^{-1}
Specific vapor-exchange rate	β_v	derived	2.0×10^{-5}	s^{-1}
Reference respiration source	Q_{r0}	30–150	110	W m^{-3}
Temperature sensitivity	γ_T	0.03–0.12	0.075	K^{-1}
Moisture sensitivity	γ_M	0–25	12	$(kg\,kg^{-1})^{-1}$
GAB monolayer moisture	M_m	0.05–0.09	0.071	kg kg^{-1}
GAB coefficients	C, K	literature-supported	8.5, 0.82	–

No independent experimental dataset was available for coefficient fitting in the present study. Consequently, the baseline values in Table 1 should be interpreted as a transparent numerical parameterization for a reproducible benchmark, not as experimentally calibrated coefficients.

Future use with measured storage data should estimate the case-specific coefficients within physically admissible bounds and report the calibration and validation datasets separately from the numerical verification presented here.

2.7. Source Terms and Equilibrium Closures

Respiration heat generation was represented by:

$$Q_r(T, M) = Q_{r0}\exp[\gamma_T(T - T_0)][1 + \gamma_M(M - M_0)],$$

where Q_{r0} is the reference respiration heat-generation rate, γ_T is the temperature-sensitivity coefficient and γ_M is the moisture-sensitivity coefficient. This bounded empirical closure is restricted to the ranges stated in Section 2.2.

The reference rate Q_{r0} represents the volumetric heat released by aerobic respiration of the grain and of associated micro-organisms. With the heat of complete glucose oxidation (about 10.6 MJ per kg of CO_2 produced), the baseline Q_{r0} = 110 W m^{-3} corresponds to 0.14 W per kg of bulk grain (≈0.16 W per kg of dry matter), or approximately 1.1 g CO_2 kg^{-1} d^{-1}. This is of the same order as the peak heat production of 0.10–0.15 W per kg of dry matter measured for wet wheat (23–27% w.b.) under adiabatic conditions [13] and is far above the respiration of sound grain at 14% d.b. [10,12]. The baseline therefore represents a biologically active hot-spot scenario; for example, a localized pocket of infested or mold-active grain, chosen so that a measurable internal maximum develops within about one day; for sound grain, the same equations apply with a proportionally smaller Q_{r0} and correspondingly longer time scales. The temperature coefficient γ_T = 0.075 K^{-1} corresponds to $Q_{10} = \exp(10\gamma_T) \approx 2.1$, a value typical of biological respiration, and γ_M represents the increase of respiration with moisture near the reference state. Because M changes by less than 10^{-3} percentage points over the simulated horizon, γ_M has a negligible influence on the present results (Section 3.10). The exponential law has no temperature optimum, whereas measured heat production of wet wheat peaks at about 43–46 °C and declines at higher temperatures [13]; the closure is therefore used only for core temperatures well below this range.

The grain-air equilibrium state was represented by the GAB relation:

$$M = \frac{M_m C K a_w}{(1 - K a_w)(1 - K a_w + C K a_w)}, \quad (2)$$

with $M_m = 0.071\ \mathrm{kg\,kg^{-1}}$, $C = 8.5$ and $K = 0.82$. For each local pair (T, M), this equation was inverted on $0 < a_w < 1$ to obtain water activity. Over the present moisture interval, it gives $a_w \approx 0.658$ at $M = 0.140$ and $a_w \approx 0.705$ at $M = 0.155$.

In the baseline model, the GAB constants M_m, C and K are held constant at values representative of wheat near 20 °C, selected within the ranges reported for wheat isotherms [20,23]. The inversion therefore gives a_w as a function of M only, and temperature enters the interfacial humidity W_i exclusively through $p_{sat}(T)$. The resulting $a_w \approx 0.66$ at $M = 0.140$ kg kg^{-1} is consistent in magnitude with the equilibrium relative humidities reported for wheat at this moisture level [20]. The temperature shift of the isotherm at constant moisture content was neglected in the baseline. Its effect was quantified a posteriori (Section 3.11) with a Clausius-Clapeyron correction, $a_w(T,M) = a_{w,GAB}(M) \exp[-(q_{st}/R)(1/T_K - 1/T_{ref,K})]$, with $T_{ref} = 20$ °C and net isosteric heat $q_{st} = 3$, 6 and 9 kJ mol^{-1}. This range lies between the near-zero net isosteric heats reported for wheat above about 14% d.b. and the ≈17 kJ mol^{-1} reported at 10% d.b. [21,40]. Sorption hysteresis was bounded by evaluating the isotherm at $M - \Delta M_h$, with $\Delta M_h = \pm 0.5$ and ± 1.0 percentage points, the order of the adsorption–desorption gap reported for cereal grains [39,41].

The equilibrium absolute humidity at the grain-air interface was calculated from:

$$W_i(T, M) = 0.622\, \frac{a_w\, p_{sat}(T)}{P - a_w\, p_{sat}(T)},$$

and the volumetric exchange term was:

$$S_v(T, M, W) = K_v[W_i(T, M) - W].$$

This closure separates solid-phase diffusion, pore air diffusion and interfacial exchange and maintains dimensional consistency in Equation (1).

2.8. Initial and Boundary Conditions

The initial state was prescribed as:

$$T(\mathbf{x}, 0) = T_0(\mathbf{x}), \qquad M(\mathbf{x}, 0) = M_0(\mathbf{x}), \qquad W(\mathbf{x}, 0) = W_0(\mathbf{x}), \qquad \mathbf{x} \in \Omega.$$

The initial fields were spatially uniform for the baseline calculation. The influence of non-uniform initial temperature and moisture fields is examined separately in Section 3.11.

At the lateral faces and the upper face, heat and pore air humidity exchange were represented by:

$$-\lambda_{eff}\frac{\partial T}{\partial n} = h_T(T - T_\infty), \qquad -D_W\frac{\partial W}{\partial n} = h_W(W - W_\infty), \qquad \mathbf{x} \in \partial\Omega_R.$$

The second relation is written after division of the gas-phase balance by $\rho_a \varepsilon$; equivalently, the physical vapor mass flux is:

$$-\rho_a \varepsilon D_W \frac{\partial W}{\partial n} = \rho_a \varepsilon h_W(W - W_\infty).$$

Thus, h_W is a mass-transfer velocity with units of m s^{-1}. In the baseline simulation, the ambient humidity ratio was prescribed directly as $W_\infty = 0.0100$ kg kg^{-1}. When measured relative humidity is available, W_∞ can instead be calculated from relative humidity, saturation vapor pressure and atmospheric pressure using the corresponding psychrometric relation.

No direct external solid-phase moisture flux was imposed:

$$-\rho_s(1 - \varepsilon)D_M\frac{\partial M}{\partial n} = 0, \qquad \mathbf{x} \in \partial\Omega_R,$$

because exchange between kernels and pore air is already represented by S_v. At the insulated and impermeable lower face:

$$\frac{\partial T}{\partial n} = 0, \qquad \frac{\partial M}{\partial n} = 0, \qquad \frac{\partial W}{\partial n} = 0, \qquad \mathbf{x} \in \partial\Omega_0.$$

2.9. Numerical Discretization

The governing equations were solved on a uniform Cartesian grid. The computational domain was divided into N_x, N_y, and N_z control volumes along the coordinate directions. The dependent variables T, M, and W were stored at cell centers, and the time interval was divided into steps of size Δt.

The diffusion operators were approximated in conservative finite-difference form. For a general scalar variable Φ with a spatially varying diffusion coefficient D_Φ, the diffusion term was approximated as:

$$\begin{aligned}\nabla \cdot (D_\Phi \nabla \Phi) \approx{}& \frac{1}{\Delta x}\left[D_{i+\frac{1}{2},j,k}\frac{\Phi_{i+1,j,k}-\Phi_{i,j,k}}{\Delta x} - D_{i-\frac{1}{2},j,k}\frac{\Phi_{i,j,k}-\Phi_{i-1,j,k}}{\Delta x}\right] \\ &+ \frac{1}{\Delta y}\left[D_{i,j+\frac{1}{2},k}\frac{\Phi_{i,j+1,k}-\Phi_{i,j,k}}{\Delta y} - D_{i,j-\frac{1}{2},k}\frac{\Phi_{i,j,k}-\Phi_{i,j-1,k}}{\Delta y}\right] \\ &+ \frac{1}{\Delta z}\left[D_{i,j,k+\frac{1}{2}}\frac{\Phi_{i,j,k+1}-\Phi_{i,j,k}}{\Delta z} - D_{i,j,k-\frac{1}{2}}\frac{\Phi_{i,j,k}-\Phi_{i,j,k-1}}{\Delta z}\right].\end{aligned} \tag{3}$$

For spatially varying coefficients, face values were calculated by harmonic averaging:

$$D_{i+1/2} = \frac{2D_i D_{i+1}}{D_i + D_{i+1}}.$$

This averaging preserves conservative fluxes across neighboring cells and is suitable for heterogeneous porous media.

Time integration was performed using an explicit forward scheme. At each time level, the effective coefficients, respiration heat source $Q_r(T, M)$, equilibrium interfacial humidity $W_i(T, M)$, and vapor exchange term $S_v(T, M, W)$ were recalculated from the current values of T, M, and W. The update equations were written as:

$$T_{i,j,k}^{n+1} = T_{i,j,k}^{n} + \Delta t\, F_T(T^n, M^n, W^n), \tag{4}$$

$$M_{i,j,k}^{n+1} = M_{i,j,k}^{n} + \Delta t\, F_M(T^n, M^n, W^n), \tag{5}$$

$$W_{i,j,k}^{n+1} = W_{i,j,k}^{n} + \Delta t\, F_W(T^n, M^n, W^n), \tag{6}$$

where F_T, F_M, and F_W denote the discrete right-hand sides of the heat, grain-moisture, and pore air humidity equations, respectively. After division by the corresponding accumulation coefficients, F_T contains $(Q_r - L_v S_v)/(\rho c)$, F_M contains $-S_v/[\rho_s(1-\varepsilon)]$, and F_W contains $+S_v/(\rho_a \varepsilon)$. The density and phase-fraction factors therefore remain present in both the continuous and discrete mass balances. All right-hand sides F_T, F_M and F_W, including the effective coefficients, the source terms Q_r and S_v and the Robin boundary fluxes, are evaluated entirely at the current time level n; no quantity at level $n+1$ appears on the right-hand side, so that Equations (4)–(6) constitute a fully explicit forward-Euler update.

The time step was selected according to the diffusion stability restriction:

$$\Delta t \le \frac{1}{2D_{max}(\Delta x^{-2} + \Delta y^{-2} + \Delta z^{-2})},$$

where:

$$D_{max} = \max(D_T, D_M, D_W).$$

For the present coefficients, this limit is about 2.95×10^4, 7.39×10^3 and 1.85×10^3 s on the coarse, base and fine grids, and the source-term time scales are $\tau_v = 2.0 \times 10^4$ s for interphase exchange and $\rho c / (Q_{r0}\gamma_T) \approx 1.8 \times 10^5$ s for the respiration feedback. The time

steps used (240, 60 and 15 s) are therefore about 120 times smaller than the stability limit; they were not dictated by stiffness but chosen proportional to Δx^2 (constant diffusion number) so that the first-order temporal error remains small compared with the spatial error on every grid (Section 3.2). Robin boundary conditions for heat and pore air humidity were implemented through boundary flux approximations, while the lower insulated and impermeable boundary was imposed by zero normal fluxes. The implementation of the lower no-flux condition was verified separately to ensure that the predicted thermal maximum was not a boundary-discretization artifact.

2.10. Numerical Verification and Diagnostic Evaluation

The numerical implementation was assessed in three complementary ways. (i) Spatial refinement used the 10 × 10 × 5, 20 × 20 × 10 and 40 × 40 × 20 grids, first with the time step scaled with Δx^2 (240, 60 and 15 s) and then with a common time step of 15 s on all grids, so that the spatial discretization error is isolated from the temporal error; the base grid was additionally run with Δt = 240, 120, 60, 30 and 15 s. Observed orders and grid convergence indices (GCI, safety factor 1.25 [42]) were computed for the mean temperature, the peak temperature, the maximum pore air humidity and the probe values, and the locations of the temperature and humidity maxima were compared across grids. (ii) The peak temperature was compared with an analytical solution for an adiabatic core (Section 3.9). (iii) Global water and energy balances were evaluated from the cumulative interphase, boundary and source terms accumulated during the time integration.

A representative numerical probe was defined at normalized coordinates $x / L_x = 0.5$, $y / L_y = 0.5$ and $z / L_z = 0.3$. This point is a diagnostic sampling location inside the computed field and is not an experimental sensor. Its simulated temperature and pore air humidity histories are reported to illustrate the transient response of the coupled model.

The baseline calculation used T_0 = 20 °C, M_0 = 0.140 kg kg^{-1} dry basis, W_0 = 0.0100 kg kg^{-1}, T_∞ = 20 °C, W_∞ = 0.0100 kg kg^{-1} and P_{atm} = 101,325 Pa in a 1.0 m × 1.0 m × 0.5 m domain. The base grid was 20 × 20 × 10 with Δt = 60 s, and the principal comparison time was 28.3 h.

Section 3.4 reports the simulated probe histories and the baseline full-field ranges and diagnostic quantities at 28.3 h. Sections 3.5–3.7 present the corresponding x–z sections through the horizontal middle of the domain. Section 3.9 summarizes the analytical check and the water budget, and Sections 3.10 and 3.11 report the sensitivity and robustness tests. Sections 3.12–3.14 report the natural-convection check, the semi-implicit time integration and the global sensitivity analysis introduced in Section 2.11.

All diagnostics are reported at t = 28.3 h (1.02 × 10^5 s). This horizon was selected for physical rather than numerical reasons: (i) it spans about five gas-phase relaxation times τ_v, so that the pore air humidity has adjusted to the local interfacial equilibrium and the initial condensation transient (Section 3.9) has decayed; (ii) it keeps the baseline core temperature near 30 °C, well below the 43–46 °C range in which the heat production of wet wheat peaks [13] and beyond which an exponential respiration law is no longer meaningful; and (iii) it lies below the finite-time runaway time of every sensitivity case (≈34 h for +50% Q_{r0}, Section 3.9). The explicit solution remains stable and time-step-independent beyond this horizon (Section 3.9), but the respiration closure then drives the core into thermal runaway (≈51 h for the baseline).

Because no independent experimental measurements are used, RMSE, MAPE or other model-data error statistics are not reported. The present evidence is therefore numerical verification rather than experimental validation. Future field or laboratory validation should use independent temperature and humidity measurements at multiple depths and locations.

2.11. Model-Form Extensions: Natural Convection, Semi-Implicit Integration and Global Sensitivity

Three extensions were added to test the main modeling choices of the benchmark. They use the same grid, parameters and boundary conditions as the baseline model, reduce exactly to it when switched off, and are included in Supplementary File S1.

Natural convection. To test the diffusion-dominated assumption (Section 2.2), the model was coupled with buoyancy-driven Darcy flow of the pore air in the Boussinesq approximation [43,44]:

$$\mathbf{u} = -\frac{\kappa}{\mu}(\nabla p' - \rho_a \beta g (T - T_0)\mathbf{e}_z), \quad \nabla \cdot \mathbf{u} = 0, \tag{7}$$

where $\mathbf{u}$ is the Darcy (superficial) velocity, κ the permeability of the grain bed, $\mu = 1.81 \times 10^{-5}$ Pa s the dynamic viscosity of air, p' the deviation of the pressure from the hydrostatic reference state, $\beta = 1 / T_0$ (absolute temperature) the thermal expansion coefficient of air, $g = 9.81$ m s^{-2} and $\mathbf{e}_z$ the upward unit vector. The advective terms $-\rho_a c_{pa} \nabla \cdot (\mathbf{u}T)$, with $c_{pa} = 1006$ J kg^{-1} K^{-1}, and $-\varepsilon^{-1} \nabla \cdot (\mathbf{u}W)$ were added to the right-hand sides of the heat and pore air humidity equations, respectively; grain moisture is immobile. Substituting Equation (7) into the continuity condition gives a Poisson equation for p', which was solved at every time step on the same grid, so that the discrete face fluxes are exactly divergence-free. Advective face fluxes were evaluated by first-order upwinding, and the time steps of Section 2.9 kept the advective Courant number below 0.47. Two airflow conditions were considered: a sealed bed with impermeable walls, floor and surface, and an open surface ($p' = 0$) through which headspace air at T_∞ and W_∞ can enter. The permeability was varied over the range measured for wheat, $\kappa = 7.29 \times 10^{-9}$–$1.15 \times 10^{-8}$ m^2 [45]. The strength of natural convection is characterized by the filtration Rayleigh number [43]:

$$\mathrm{Ra} = \frac{\rho_a^2 c_{pa} g \beta \kappa H \Delta T}{\mu \lambda_{\mathrm{eff}}}, \tag{8}$$

where $H = L_z$ is the bed depth and ΔT the internal temperature rise. In a horizontal porous layer heated from below, convection sets in at $\mathrm{Ra} = 4\pi^2 \approx 39.5$ [43]; when the walls are cooled, as here, a weak circulation exists at any Ra, and its intensity increases with Ra.

Semi-implicit time integration. As an alternative to the explicit update of Equations (4)–(6), a semi-implicit Crank-Nicolson/Adams-Bashforth (CNAB2) scheme was implemented on the same spatial discretization [46]. For each field $\Phi \in \{T, M, W\}$, the linear part of the right-hand side, i.e., the conservative diffusion operator with its Robin boundary terms, $A_\Phi \Phi + b_\Phi$, and, for W, the relaxation term $-K_v W / (\rho_a \varepsilon)$, is integrated with the Crank-Nicolson rule, and the remaining nonlinear part N_Φ (respiration and latent heat and the equilibrium term $K_v W_i(T, M)$) with the second-order Adams-Bashforth rule:

$$\left(I - \frac{\Delta t}{2} A_\Phi\right) \Phi^{n+1} = \left(I + \frac{\Delta t}{2} A_\Phi\right) \Phi^n + \Delta t b_\Phi + \Delta t \left(\frac{3}{2} N_\Phi^n - \frac{1}{2} N_\Phi^{n-1}\right), \tag{9}$$

where I is the identity matrix. Temperature-dependent diffusivities are evaluated at t^n. The scheme is unconditionally stable with respect to diffusion and formally second-order accurate for the temperature equation, whose conductivity is constant; lagging the weakly temperature-dependent diffusivities of M and W reduces the formal order of those equations to one. Each step requires three sparse linear solves: the constant temperature matrix is factorized once, and the symmetric positive-definite M and W systems are solved by Jacobi-preconditioned conjugate gradients. Alternating-direction-implicit or locally one-dimensional splitting [47] would reduce these solves to tridiagonal systems.

Global sensitivity analysis. The one-at-a-time and factorial analyses (Section 3.10) were complemented by a variance-based global sensitivity analysis [48,49]. Six parameters were treated as independent, uniformly distributed inputs: Q_{r0}, γ_T and λ_g within ±25% and

K_v, h_T and h_W within ±50% of their baseline values. The narrower range of the respiration parameters keeps every sample below the finite-time runaway time at 28.3 h (Section 3.9). For an output Y (T_{peak}, W_{max} or the mean temperature T_{mean}), the first-order and total Sobol' indices of an input X_i are:

$$S_i = \frac{V[E(Y|X_i)]}{V(Y)}, \quad S_{Ti} = \frac{E[V(Y|X_{\sim i})]}{V(Y)}, \tag{10}$$

where $X_{\sim i}$ denotes all inputs except X_i; S_i measures the share of the output variance caused by X_i alone and $S_{Ti} - S_i$ the share caused by its interactions with the other inputs. The indices were estimated with the Saltelli sampling design and the Saltelli and Jansen estimators [50] from $N = 512$ base samples of a scrambled Sobol' sequence, i.e., $N(k + 2) = 4096$ model runs for $k = 6$, and 95% confidence intervals were obtained from 1000 bootstrap replicates. These runs used the semi-implicit scheme with $\Delta t = 900$ s on the base grid, whose time-integration error (about 0.001 °C, Section 3.13) is negligible compared with the parameter-induced variations.

3. Results

3.1. Baseline Parameterization and Computational Configuration

The complete parameter set used in the reported simulations is given in Table 1. The values represent prescribed baseline conditions, literature-supported material properties, derived effective quantities and case-specific coefficients used for the numerical benchmark. No coefficient in Table 1 is presented as fitted to an external monitoring dataset.

The computational domain was 1.0 m × 1.0 m × 0.5 m, the base grid contained 20 × 20 × 10 cells, and the baseline time step was 60 s. Figure 1 summarizes the state variables, source terms and boundary conditions.

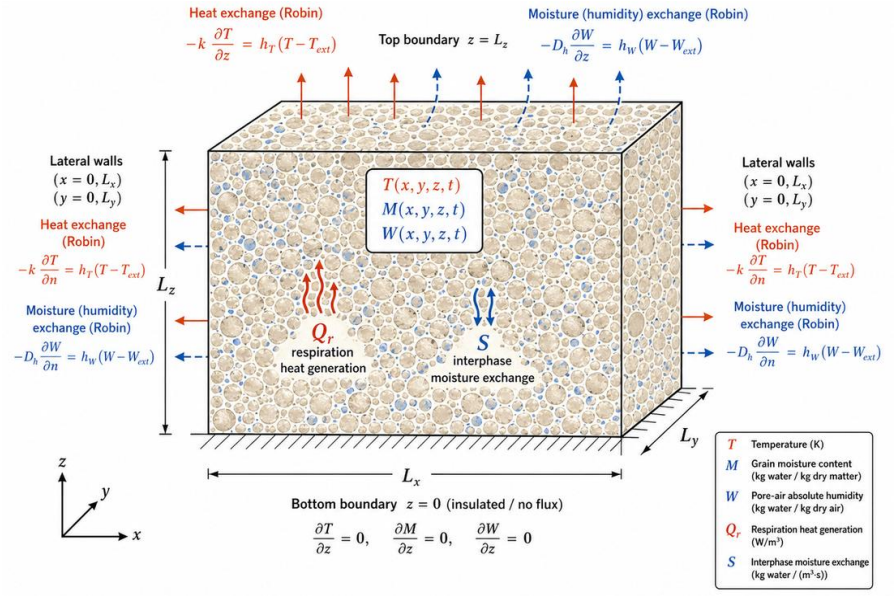


Figure 1. Schematic representation of the three-dimensional coupled model. The state variables are temperature T, grain moisture M and pore air humidity W; Q_r is respiration heat generation. The symbol S shown in the schematic denotes the volumetric interphase vapor-exchange term S_v used in the governing equations. Robin conditions act on the lateral and upper faces, and the lower face is insulated and impermeable. In the schematic, solid red arrows denote heat exchange and dashed blue arrows denote moisture (humidity) exchange through the Robin faces; the wavy red arrows indicate respiration heat generation, and the blue double-headed arrows indicate interphase

moisture exchange between the grain and the pore air. The symbols k, D_h, T_{ext} and W_{ext} used in the schematic correspond to λ_{eff}, D_W, T_∞ and W_∞ in the text, respectively.

3.2. Grid and Time-Step Refinement Assessment

Three grid levels were considered: 10 × 10 × 5 (Δ = 10 cm), 20 × 20 × 10 (Δ = 5 cm) and 40 × 40 × 20 (Δ = 2.5 cm). With the time step scaled as $\Delta t \propto \Delta^2$ (240, 60 and 15 s), the mean temperatures at 28.3 h were 28.53, 28.21 and 28.11 °C, the peak temperatures 30.71, 30.72 and 30.73 °C, and the maximum pore air humidities 15.78, 15.79 and 15.79 g kg^{-1}. The base-to-fine differences are 0.36% for the mean temperature and 0.01% and 0.02% for the peak temperature and maximum humidity, respectively (Table 2).

To separate spatial and temporal errors, the three grids were rerun with the same time step Δt = 15 s. The mean temperatures (28.54, 28.21 and 28.11 °C) are practically identical to the scaled-step values, and the observed order based on the mean temperature, p = 1.70, is unchanged, with a fine-grid GCI of 0.20%. The mean-temperature error is therefore spatial and is dominated by the thin thermal boundary layer near the Robin faces: the thermal penetration depth $(D_T t)^{1/2} \approx 0.08$ m at 28.3 h is smaller than the coarse-grid spacing (10 cm), so the coarse grid lies outside the asymptotic range, which explains why p is below the formal second order of Equation (3). The peak temperature and maximum humidity, located in the interior far from the cooled faces, converge much faster: with Δt = 15 s, their base-to-fine differences and fine-grid GCIs are below 0.01%.

On the base grid, reducing Δt from 240 to 15 s changes the mean temperature by 0.01 °C and the peak temperature and maximum humidity by 0.01 °C and 0.01 g kg^{-1}, respectively, and the differences decrease approximately in proportion to Δt, as expected for the first-order forward-Euler scheme; at the production step Δt = 60 s, the temporal error in T_{peak} is below 0.01 °C.

The locations of the temperature and humidity maxima coincide on all grids: both lie in the lowest central cell, whose center moves from (x / L_x, y / L_y, z / L_z) = (0.45, 0.45, 0.10) on the coarse grid to (0.48, 0.48, 0.05) on the base grid and (0.49, 0.49, 0.03) on the fine grid, i.e., towards the bottom center of the domain as the cells become smaller. The reported hot-spot position is therefore grid-independent up to the cell size. The base grid (20 × 20 × 10, Δt = 60 s) was retained for the subsequent calculations because it reproduces the fine-grid peak values within 0.01% at about one-twentieth of the computing time (Table 2).

Table 2. Grid and time-step refinement results at t = 28.3 h. Upper block: time step scaled with Δ^2; lower block: common time step Δt = 15 s, which isolates the spatial discretization error. In all cases, the temperature and humidity maxima lie in the lowest central cell. CPU time is the wall-clock time on a single core (Python 3.12/NumPy). Observed order for the mean temperature: p = 1.70 (both blocks).

Grid	Δt, s	Mean T, °C	T_{peak}, °C	W_{max}, g kg^{-1}	CPU Time, s
Coarse, 10 × 10 × 5	240	28.53	30.71	15.78	0.21
Base, 20 × 20 × 10	60	28.21	30.72	15.79	1.77
Fine, 40 × 40 × 20	15	28.11	30.73	15.79	35.43
Coarse, 10 × 10 × 5	15	28.54	30.72	15.79	3.82
Base, 20 × 20 × 10	15	28.21	30.73	15.79	7.46
Fine, 40 × 40 × 20	15	28.11	30.73	15.79	36.61

3.3. Discrete Enforcement of the Lower No-Flux Boundary

The lower boundary at z = 0 is implemented as an insulated and impermeable face. In the conservative discrete operator, no external heat, grain-moisture or vapor flux is added at this lower z face, whereas Robin fluxes are applied only at the upper z face and the lateral faces.

Accordingly, the discrete normal flux through the lower face is zero by construction. This implementation is independent of the internal source terms and prevents artificial heat or moisture removal through the base of the domain.

At 28.3 h, the maximum temperature occurs in the lowest central cell, at approximately (x / L_x, y / L_y, z / L_z) = (0.48, 0.48, 0.05). This location is consistent with volumetric heat generation combined with heat removal through the lateral and upper surfaces and insulation at the bottom.

3.4. Transient Response at a Representative Internal Probe

Figure 2 shows the simulated temperature and pore air humidity histories at the representative internal probe (x / L_x, y / L_y, z / L_z) = (0.5, 0.5, 0.3). At 28.3 h, the probe temperature reaches 30.72 °C, and the pore air humidity reaches 15.79 g kg^{-1}. The grain moisture at the same point remains at 14.00% d.b. (a decrease of 3.5 × 10^{-4} percentage points), confirming that the gas-phase humidity responds much more strongly than the solid-phase moisture over this short simulation horizon.

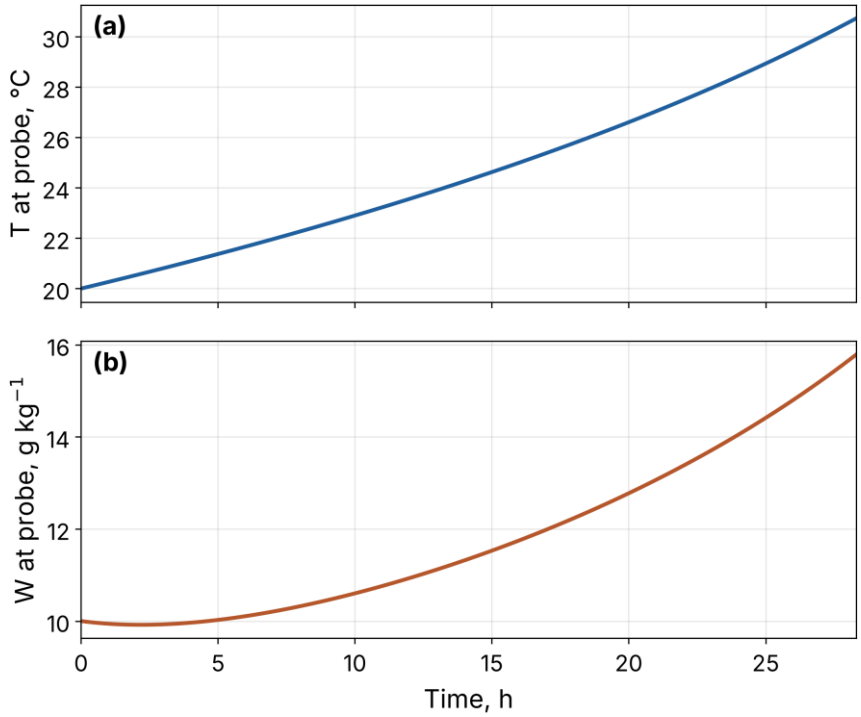


Figure 2. Simulated temporal evolution of (**a**) temperature and (**b**) pore air absolute humidity at the representative numerical probe located at x / L_x = 0.5, y / L_y = 0.5 and z / L_z = 0.3 over 28.3 h. The probe is a computational sampling point, not an experimental sensor.

Table 3 confirms the separation of timescales in the baseline case: temperature and pore air humidity change substantially, whereas grain moisture remains almost unchanged. These are simulated quantities only; no model-data error metrics are reported.

Table 3. Baseline full-field and diagnostic quantities at t = 28.3 h.

Variable	Initial	Range at 28.3 h	Indicator
Temperature, T	20.00 °C	21.71–30.72 °C	Peak at z / L_z = 0.05
Grain moisture, M	14.00% d.b.	14.00% d.b.	ΔM from −3.5 × 10^{-4} to −0.5 × 10^{-4} pp

Pore air humidity, W	10.00 g kg^{-1}	10.39–15.79 g kg^{-1}	Lower-central maximum

3.5. Temperature Distribution and Formation of the Internal Thermal Maximum

The computed temperature field develops a broad internal warm region. Starting from a uniform 20 °C state, respiration heat generation raises the interior temperature while heat is removed through the lateral and upper boundaries. Because the bottom is insulated, the warmest region shifts toward the lower central part of the domain.

At 28.3 h, the base-grid temperature ranges from 21.71 to 30.72 °C, with a domain mean of 28.21 °C. The maximum occurs in the lowest central cell near (x / L_x, y / L_y, z / L_z) = (0.48, 0.48, 0.05). Figure 3a shows the middle x–z section: the lower-central portion remains warmest, while the lateral and upper layers are cooler because of boundary exchange.

This lower-central maximum is a direct consequence of the stated model assumptions and boundary conditions. It should be interpreted as a feature of the diffusion-dominated benchmark rather than as a universally predicted hot-spot position for real silos, where airflow and asymmetric wall forcing may shift the thermal maximum.

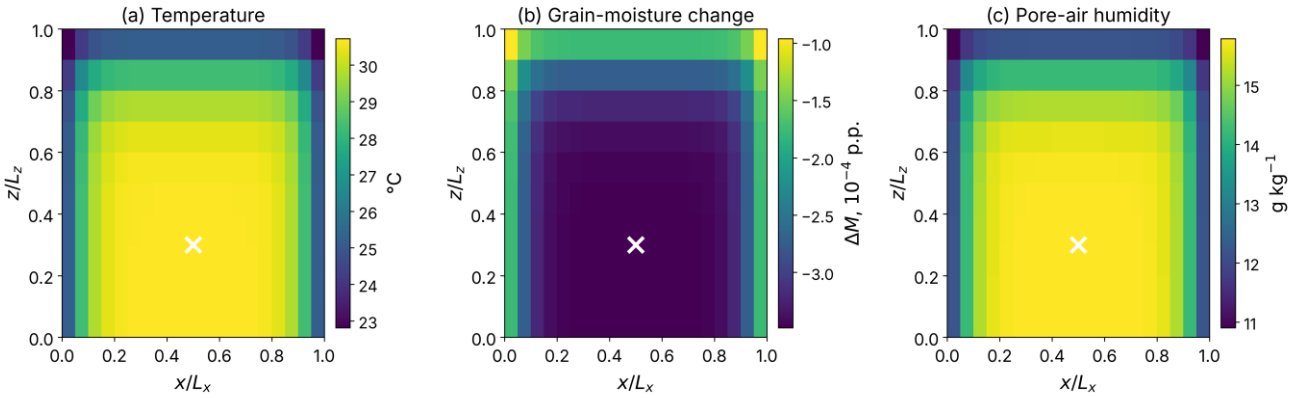


Figure 3. Simulated x–z distributions through the horizontal middle of the grain bed at t = 28.3 h: (**a**) temperature, (**b**) grain-moisture change relative to the initial 14.00% d.b., and (**c**) pore air absolute humidity. The white × marks the representative numerical probe at x / L_x = 0.5 and z / L_z = 0.3; it does not mark the field maximum.

3.6. Grain-Moisture Redistribution

The grain-moisture field changes extremely slowly over 28.3 h. The warmer interior promotes a small net transfer of moisture from the solid phase to the pore air, but the low grain-moisture diffusivity and short time horizon prevent appreciable redistribution within the kernels.

The full-field grain moisture remains within 14.00% d.b. to two decimal places; relative to the initial 14.00% d.b., the local changes range from -3.5×10^{-4} to -0.5×10^{-4} percentage points. Figure 3b visualizes this very small spatial variation without implying a practically significant moisture-content change.

This result demonstrates a strong timescale separation: solid-phase moisture responds far more slowly than temperature and pore air humidity in the present parameterization. For longer storage periods or larger grain-moisture diffusivity, the solid-phase redistribution would be expected to become more visible.

3.7. Pore Air Humidity Distribution

Pore air absolute humidity responds much more rapidly than grain moisture. At 28.3 h, the full-field humidity ranges from 10.39 to 15.79 g kg^{-1}, compared with the initial value of 10.00 g kg^{-1}. The maximum occurs in the same lower-central region as the thermal maximum.

Figure 3c shows that vapor accumulation follows the warmer internal region, whereas the lateral and upper layers remain less humid because of diffusion and boundary exchange. This coupling makes pore air humidity a more responsive short-time indicator of the simulated internal state than bulk grain moisture.

The contrast between M and W is therefore pronounced: M changes by less than 4 × 10^{-4} percentage points, while W increases by several grams per kilogram in the core. The two variables should not be treated as interchangeable moisture measures.

The temperature and pore air humidity maxima are displaced toward the insulated lower boundary, whereas grain moisture remains nearly uniform. The fields therefore show strong thermal and gas-phase evolution but only a negligible short-time change in the solid-phase moisture content.

The contrast between W and M follows directly from the water-storage capacities of the two phases. Per unit bulk volume, the solid phase contains $\rho_s(1-\varepsilon)$ = 798 kg of dry matter, whereas the pore air contains only $\rho_a\varepsilon$ = 0.48 kg of dry air, a ratio of about 1.66 × 10^3. Transferring 1 g of water from the grain to the pore air in the 0.5 m^3 domain therefore raises the mean W by 4.17 g kg^{-1} but lowers the mean M by only 2.5 × 10^{-4} percentage points. Over 28.3 h the grain released 1.08 g of water (time integral of S_v over the domain), of which 1.00 g remained in the pore air, and 0.08 g left through the Robin faces (Figure 4b); the corresponding mean changes, ΔW = +4.18 g kg^{-1} and ΔM = −2.7 × 10^{-4} percentage points, agree with the field values in Table 3. During the first ≈5 h, the pore air is slightly above the interfacial equilibrium (W_0 = 10.00 g kg^{-1} versus $W_i \approx$ 9.57 g kg^{-1} at 20 °C), so that a small amount of vapor is first taken up by the grain before warming reverses the exchange. The large humidity increase is therefore consistent with an almost imperceptible change in grain moisture.

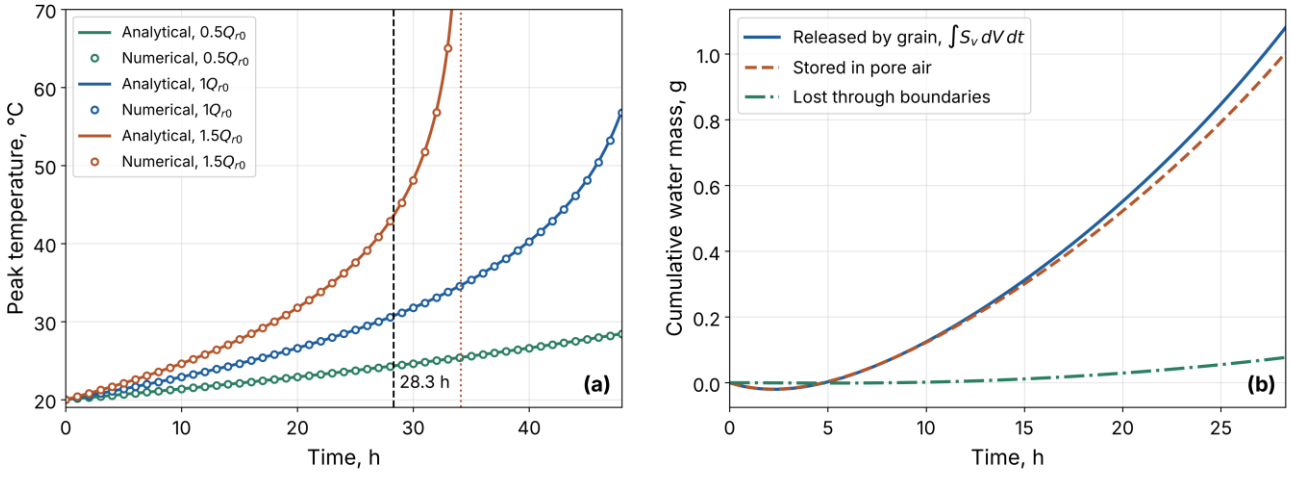


Figure 4. (**a**) Peak temperature versus time for 0.5, 1.0 and 1.5 times the reference respiration source: numerical solution (symbols) and analytical adiabatic-core solution (lines). Dotted vertical lines mark the runaway time t^* where it lies within the plotted interval; the dashed line marks the 28.3 h reporting horizon. (**b**) Cumulative water budget of the baseline case: water released by the grain, water stored in the pore air and water lost through the Robin faces; the global water balance closes to machine precision.

3.8. Coupled Interpretation of Heat and Moisture Dynamics

The combined analysis of T, M and W reveals three distinct response scales. Temperature increases over hours because of respiration heat generation and limited diffusion to the boundaries. Pore air humidity responds rapidly to changes in temperature and interfacial equilibrium. Grain moisture changes only minimally over the 28.3 h horizon.

Consequently, a relatively small solid-phase moisture change can coexist with substantial internal warming and vapor accumulation. In the present benchmark, the lower-central region reaches the highest T and W values, while the exposed boundary layers remain cooler and less humid.

The short-time coupling is therefore dominated by the thermal source and gas-phase response. Moisture still enters the respiration and equilibrium closures, but its own field changes too slowly to provide strong feedback over the simulated interval.

3.9. Analytical Check of the Respiration Source and Global Water and Energy Balances

Because the hot spot lies in the insulated lower-central region, farther from the cooled faces than the thermal penetration depth (≈0.08 m), the core heats almost adiabatically. Neglecting diffusion and the small latent and moisture terms, the heat equation reduces there to $\rho c\, \mathrm{d}\theta / \mathrm{d}t = Q_{r0} \exp(\gamma_T \theta)$, with $\theta = T - T_0$, whose solution is $\theta(t) = -\gamma_T^{-1} \ln(1 - t / t^*)$, where $t^* = \rho c / (Q_{r0}\gamma_T)$. The temperature therefore grows faster than linearly and diverges at the finite runaway time t^*, which equals 102, 51 and 34 h for 0.5, 1.0 and 1.5 times the baseline Q_{r0}. At 28.3 h, the analytical solution gives 24.32, 30.73 and 43.58 °C, compared with numerical peak temperatures of 24.31, 30.72 and 43.52 °C (Figure 4a). The agreement to within about 0.01 °C for the baseline (0.06 °C for the most intense case, in which boundary losses and latent cooling begin to matter) verifies the implementation of the respiration source and its coupling to the heat equation.

The global balances were evaluated from the cumulative boundary fluxes and volumetric sources. Over 28.3 h, the respiration source released 7.62 MJ, of which 1.39 MJ left through the Robin faces, 2.65 kJ was consumed as latent heat, and 6.24 MJ remained as sensible heat in the bed; the energy balance closes with a residual of 4×10^{-9} J. The total water inventory (55.86 kg) changes only by the 0.08 g lost through the boundaries, and the water balance closes with a residual below 10^{-13} kg, i.e., to machine precision (Figure 4b). These residuals confirm that the conservative discretization and the opposite-sign treatment of S_v conserve water and energy at the discrete level.

3.10. Sensitivity of Storage-Risk Indicators

A one-at-a-time sensitivity analysis was performed at t = 28.3 h. Each selected parameter was changed by ±50% while all others were held fixed. The primary response quantities were peak temperature and maximum pore air humidity; the mean grain-moisture change was also checked and remained below 10^{-3} percentage points in all tested cases. In the revised analysis, the set of perturbed parameters was extended to the effective diffusivities D_{W0} and D_{M0}, the respiration sensitivities γ_T and γ_M, and the grain thermal conductivity λ_g (Table 4).

Over this short diffusion-dominated horizon, changing the boundary heat-transfer coefficient h_T by ±50% changes the peak temperature by less than 10^{-4} °C. The boundary vapor-transfer coefficient h_W likewise has a negligible effect on the maximum internal humidity. This occurs because the low effective diffusivities limit the penetration of boundary forcing into the core over 28.3 h.

The reference respiration source Q_{r0} is the dominant thermal parameter. Increasing Q_{r0} by 50% raises the peak temperature by 12.79 °C and the maximum pore air humidity by 9.96 g kg^{-1}, whereas decreasing it by 50% lowers these quantities by 6.41 °C and 3.97 g kg^{-1}, respectively. The asymmetry is a direct consequence of the exponential respiration

feedback (Section 3.9): the core temperature rise $\theta = -\gamma_T^{-1} \ln(1 - t / t^*)$ depends nonlinearly on Q_{r0} through $t^* \propto 1 / Q_{r0}$. At 28.3 h, $t / t^* = 0.28$, 0.55 and 0.83 for 0.5, 1.0 and 1.5 Q_{r0}, so that the +50% case approaches runaway whereas the −50% case remains in an almost linear regime. The local elasticity $\partial \ln\theta / \partial \ln Q_{r0} = (t / t^*)/[(1 - t / t^*)(-\ln(1 - t / t^*))]$ equals 1.54 for the baseline; a 10% uncertainty in Q_{r0} thus produces about a 15% uncertainty in the predicted temperature rise, and this amplification grows without bound as t approaches t^*. The temperature coefficient γ_T acts in the same way (+4.96 and −2.10 °C for ±50%).

The interphase vapor-transfer coefficient K_v primarily controls the gas-phase humidity response: a +50% change increases W_{max} by 0.70 g kg^{-1}, whereas a −50% change decreases W_{max} by 1.50 g kg^{-1}; its effect on peak temperature remains below 0.01 °C. These results distinguish source-driven thermal sensitivity from interphase-control of vapor accumulation.

Table 4. One-at-a-time sensitivity analysis at t = 28.3 h. Changes are relative to the baseline T_{peak} = 30.72 °C and W_{max} = 15.79 g kg^{-1}; "<0.01" denotes an absolute change smaller than 0.01.

Parameter	Variation	ΔT_{peak}, °C	ΔW_{max}, g kg^{-1}
h_T	±50%	<0.01	<0.01
h_W	±50%	<0.01	<0.01
K_v	+50%	<0.01	+0.70
K_v	−50%	<0.01	−1.50
Q_{r0}	+50%	+12.79	+9.96
Q_{r0}	−50%	−6.41	−3.97
γ_T	+50%	+4.96	+2.76
γ_T	−50%	−2.10	−1.22
γ_M	±50%	<0.01	<0.01
D_{M0}	±50%	<0.01	<0.01
D_{W0}	±50%	<0.01	<0.01
D_{W0}	×10	<0.01	−0.01
D_{W0}	×100	<0.01	−1.00
D_{W0}	×335 (molecular limit)	<0.01	−2.30
λ_g	0.17 and 0.21 W m^{-1} K^{-1}	<0.01	<0.01

The sensitivity results show that, for the present short-time benchmark, respiration intensity rather than boundary heat transfer governs the core temperature rise, while K_v governs a substantial part of the pore air humidity response. This conclusion is specific to the chosen geometry, transport coefficients and 28.3 h horizon and should not be generalized to longer storage periods without additional analysis.

Because one-at-a-time perturbations cannot reveal synergistic or antagonistic effects, a two-level full factorial design (2^4 = 16 runs, ±50%) was additionally evaluated for h_T, K_v, Q_{r0} and h_W. For T_{peak}, the main effect of Q_{r0} (19.21 °C, high minus low level) dominates, and all interaction effects are below 0.01 °C, so that the thermal response is effectively additive in these parameters. For W_{max}, however, the $K_v \times Q_{r0}$ interaction effect (3.25 g kg^{-1}) is of the same order as the main effect of K_v (3.92 g kg^{-1}): stronger respiration raises the interfacial equilibrium humidity, and K_v controls how closely the pore air follows it, so that the humidity response is markedly synergistic. Interactions involving h_T and h_W are negligible. One-at-a-time indices are therefore adequate for the thermal indicator but understate the joint influence of K_v and Q_{r0} on pore air humidity; this joint influence is quantified by the variance-based global sensitivity analysis in Section 3.14.

3.11. Robustness to Closure Assumptions and Initial Conditions

Table 5 summarizes three groups of additional runs that address assumptions which cannot be removed without experimental data: the temperature independence of the sorption isotherm, sorption hysteresis and spatially uniform initial fields.

The Clausius-Clapeyron correction of Section 2.7 raises the interfacial equilibrium humidity in the warm core: W_{max} increases by 0.56, 1.14 and 1.75 g kg^{-1} (3.6–11.1%) for q_{st} = 3, 6 and 9 kJ mol^{-1}, whereas T_{peak} changes by less than 0.01 °C and the locations of the maxima are unchanged. Neglecting the temperature shift of the isotherm therefore underestimates the core humidity by up to about 11% in this range but does not affect the thermal results.

A desorption-type hysteresis shift (grain at a given M in equilibrium with a lower a_w) reduces W_{max} by 0.43 and 0.89 g kg^{-1} for ΔM_h = 0.5 and 1.0 percentage points, and an adsorption-type shift increases it by 0.41 and 0.80 g kg^{-1}; T_{peak} changes by at most 0.01 °C. The cumulative grain-to-air water transfer changes by −21% to +19%, while the latent heat remains below 0.04% of the respiration heat.

Three non-uniform initial states were tested: a Gaussian warm pocket of +2 K (standard deviation 0.10 m) centered off-axis at (x, y, z) = (0.30, 0.30, 0.25) m; the same pocket with an additional +1 percentage point of grain moisture; and a linear vertical temperature stratification from 18 °C at the bottom to 22 °C at the top. In the first two cases, the hot spot no longer forms at the bottom center but at the pocket, at normalized coordinates (0.33, 0.33, 0.45), with T_{peak} = 32.13 and 33.34 °C (+1.40 and +2.61 °C) and W_{max} = 17.04 and 18.67 g kg^{-1}. In the stratified case, the maximum moves upward to z / L_z = 0.65 (T_{peak} = 31.43 °C). Locally, the 2 K initial excess becomes 1.44 K at 28.3 h despite diffusive spreading; for an adiabatic core the same excess would grow to 4.98 K, because the initial warming shortens the local runaway time by the factor $\exp(-\gamma_T \Delta T_0)$ = 0.86. The uniform initial state thus determines both the position and the magnitude of the predicted hot spot.

Table 5. Robustness of the storage-risk indicators at t = 28.3 h to the sorption closure and to non-uniform initial fields. The location refers to the cell of maximum temperature, which coincides with the cell of maximum humidity in all cases.

Case	T_{peak}, °C	W_{max}, g kg^{-1}	Location (x / L_x, y / L_y, z / L_z)
Baseline	30.72	15.79	(0.48, 0.48, 0.05)
Isotherm T-correction, q_{st} = 3 kJ mol^{-1}	30.72	16.35	(0.48, 0.48, 0.05)
Isotherm T-correction, q_{st} = 6 kJ mol^{-1}	30.72	16.93	(0.48, 0.48, 0.05)
Isotherm T-correction, q_{st} = 9 kJ mol^{-1}	30.72	17.54	(0.48, 0.48, 0.05)
Hysteresis, desorption-type, ΔM_h = +0.5 pp	30.73	15.36	(0.48, 0.48, 0.05)
Hysteresis, desorption-type, ΔM_h = +1.0 pp	30.73	14.90	(0.48, 0.48, 0.05)
Hysteresis, adsorption-type, ΔM_h = −0.5 pp	30.72	16.20	(0.48, 0.48, 0.05)
Hysteresis, adsorption-type, ΔM_h = −1.0 pp	30.72	16.59	(0.48, 0.48, 0.05)
Initial warm pocket, +2 K	32.13	17.04	(0.33, 0.33, 0.45)
Initial warm and moist pocket, +2 K, +1 pp	33.34	18.67	(0.33, 0.33, 0.45)
Initial vertical stratification, 18–22 °C	31.43	16.46	(0.48, 0.48, 0.65)

3.12. Natural-Convection Check with Darcy-Boussinesq Airflow

With the baseline temperature rise ΔT = 10.72 K and H = 0.5 m, Equation (8) gives Ra = 1.2–1.9 for the measured permeability range of wheat, more than an order of magnitude

below the onset value for bottom heating. Table 6 compares the coupled simulations with the diffusion-only model. The induced circulation is weak: warm air rises slowly in the core, spreads outward below the surface and descends along the cooled walls, with maximum Darcy velocities of 0.08–0.13 mm s^{-1}. Because the volumetric heat capacity of the pore air is about 1/1260 of that of the grain bed, the heat advected by this flow is negligible over 28.3 h: T_{peak} changes by less than 0.002 °C and the thermal maximum remains at the bottom center on all grids.

The pore air humidity, in contrast, is carried by the air itself, and its effective diffusivity is small (D_{W0} = 2.0 × 10^{-8} m^2 s^{-1}), so that the vapor Péclet number $|\mathbf{u}|H / (\varepsilon D_W)$ is of order 10^3–10^4. Natural convection therefore redistributes the vapor: W_{max} decreases by 0.22–0.48 g kg^{-1} (1.4–3.1%) in the sealed bed and by 0.75–1.64 g kg^{-1} (4.8–10.4%) with an open surface, and the humidity maximum moves from the bottom center to the upper part of the bed (z / L_z = 0.65–0.85). Humid air rising from the warm core is cooled below the surface, where part of its vapor is re-adsorbed: the maximum grain moisture content rises above its initial value by up to 2.7 × 10^{-4} percentage points, the onset of the convective moisture migration known from stored grain [44]. The vapor redistribution is consistent across grids: W_{max} varies by 0.06 g kg^{-1} (sealed) and 0.31 g kg^{-1} (open surface) between the coarse, base and fine grids, the larger spread reflecting the numerical diffusion of first-order upwinding (fine-grid reduction 8.9% for the open surface).

The diffusion-dominated treatment is therefore justified for heat transfer in a bed of this size over this horizon, but only approximately for pore air vapor: for the humidity indicator the diffusion-only model gives an upper bound at the hot spot and misses the upward displacement of the humid zone. Because Ra ∝ $\kappa H \Delta T$, convection strengthens with bed depth; for ΔT = 10 K, Ra reaches 39.5 at H ≈ 11–17 m, i.e., in commercial bins and silos, where natural convection also controls the position of the thermal maximum [31,32,44].

Table 6. Natural-convection check at t = 28.3 h (base grid unless stated). κ: permeability of the grain bed; location of the humidity maximum in normalized coordinates (x / L_x, y / L_y, z / L_z); $|u|_{max}$: maximum Darcy velocity. The temperature maximum is at the bottom center in all cases.

Airflow Condition	κ, 10^{-8} m^2	T_{peak}, °C	W_{max}, g kg^{-1}	Location of W_{max}	$\|u\|_{max}$, mm s^{-1}
Diffusion only (baseline)	–	30.72	15.79	(0.48, 0.48, 0.05)	–
Sealed	0.73	30.72	15.57	(0.48, 0.48, 0.65)	0.075
Sealed	1.15	30.72	15.31	(0.48, 0.48, 0.75)	0.119
Open surface	0.73	30.72	15.04	(0.53, 0.53, 0.75)	0.083
Open surface	1.15	30.72	14.15	(0.53, 0.53, 0.85)	0.131
Diffusion only, coarse grid	–	30.71	15.78	(0.45, 0.45, 0.10)	–
Sealed, coarse grid	1.15	30.71	15.30	(0.55, 0.55, 0.70)	0.066
Open surface, coarse grid	1.15	30.71	14.08	(0.55, 0.45, 0.70)	0.079
Diffusion only, fine grid	–	30.73	15.79	(0.49, 0.49, 0.03)	–
Sealed, fine grid	1.15	30.73	15.36	(0.51, 0.49, 0.73)	0.146
Open surface, fine grid	1.15	30.73	14.39	(0.49, 0.51, 0.83)	0.159

3.13. Semi-Implicit Crank-Nicolson Integration

Table 7 compares the semi-implicit CNAB2 solution with the explicit scheme. Since the explicit results are first-order in time, their Richardson extrapolation from Δt = 120 and 60 s, T_{peak} = 30.7283 °C, serves as a reference. The CNAB2 results converge to this limit: for Δt = 60 and 300 s, they agree with it to within 0.0002 °C, and for Δt = 900 s, fifteen times the explicit base-grid step, the error is 0.0011 °C, about four times smaller than that of the explicit scheme at Δt = 60 s (0.0039 °C). The observed temporal order between 900, 1800 and 3600 s is 1.7–2.3. The scheme remains stable at Δt = 7200 s, 120 times the explicit step,

with an error of 0.063 °C. On the fine grid, CNAB2 with Δt = 900 s reproduces the explicit result (Δt = 15 s) to 0.0001 °C in 13.8 s instead of 20.1 s, and the advantage grows with refinement: the explicit cost scales as N^5, whereas the semi-implicit cost at a fixed, accuracy-driven step grows only with the number of unknowns and solver iterations.

The semi-implicit solver therefore removes the diffusive time-step restriction and allows steps to be chosen for accuracy, as needed for storage periods of weeks to months, and it independently confirms that the explicit benchmark results are free of time-integration artefacts.

Table 7. Comparison of explicit and semi-implicit time integration at t = 28.3 h (base grid unless stated). Errors are relative to the Richardson extrapolation of the explicit results for Δt = 120 and 60 s. Runtimes refer to one core of the same computer. They were measured in a separate session from the CPU times in Table 2 and should be compared only within this table.

Scheme	Δt, s	T_{peak}, °C	Error in T_{peak}, °C	W_{max}, g kg^{-1}	Runtime, s
Explicit (forward Euler)	240	30.7128	−0.0155	15.778	0.24
Explicit (forward Euler)	120	30.7205	−0.0078	15.785	0.43
Explicit (forward Euler)	60	30.7244	−0.0039	15.788	0.89
Explicit, Richardson limit	0	30.7283	0	15.792	–
Semi-implicit CNAB2	60	30.7283	0.0000	15.792	5.43
Semi-implicit CNAB2	300	30.7282	−0.0001	15.792	1.20
Semi-implicit CNAB2	900	30.7272	−0.0011	15.790	0.46
Semi-implicit CNAB2	1800	30.7230	−0.0053	15.781	0.27
Semi-implicit CNAB2	3600	30.7109	−0.0174	15.764	0.17
Semi-implicit CNAB2	7200	30.6653	−0.0630	15.699	0.13
Explicit, fine grid	15	30.7275	–	15.791	20.05
Semi-implicit CNAB2, fine grid	900	30.7274	–	15.790	13.78

3.14. Variance-Based Global Sensitivity Analysis

Over the sampled parameter space, T_{peak} ranges from 26.66 to 40.76 °C (standard deviation 2.78 °C) and W_{max} from 12.54 to 23.36 g kg^{-1} (standard deviation 1.95 g kg^{-1}). Table 8 shows that the two respiration parameters account for almost the entire variance of the peak temperature: S_{Ti} = 0.87 for Q_{r0} and 0.16 for γ_T, whereas the boundary coefficients and the grain conductivity contribute less than 0.001. The sum of the first-order indices, 0.96, shows that about 4% of the variance arises from the interaction of Q_{r0} and γ_T, which is expected because both enter the runaway time $t^* = \rho c / (Q_{r0}\gamma_T)$ as a product (Section 3.9).

The maximum humidity is controlled by the respiration parameters through the core temperature (S_{Ti} = 0.79 and 0.12) and by the interphase coefficient K_v (S_i = 0.11, S_{Ti} = 0.13); the boundary coefficients remain unimportant over this horizon. The global analysis thus confirms the ranking of the local and factorial analyses over a parameter space in which all inputs vary simultaneously. For calibration, the respiration parameters should be identified first, from heat-production or CO_2 data, and K_v next, from simultaneous temperature and pore air humidity measurements.

Table 8. First-order (S_i) and total (S_{Ti}) Sobol' indices at t = 28.3 h (N = 512, 4096 runs). Half-widths of the 95% bootstrap confidence intervals are at most 0.10.

Parameter	Range	S_i (T_{peak})	S_{Ti} (T_{peak})	S_i (W_{max})	S_{Ti} (W_{max})
Q_{r0}	±25%	0.832	0.869	0.747	0.790
γ_T	±25%	0.129	0.165	0.089	0.122
K_v	±50%	<0.001	<0.001	0.107	0.127

h_T	±50%	<0.001	<0.001	<0.001	<0.001
h_W	±50%	<0.001	<0.001	<0.001	<0.001
λ_g	±25%	<0.001	<0.001	<0.001	<0.001

3.15. Implications for Storage-Risk Screening

The simulation suggests two useful numerical screening quantities within the stated assumptions: the peak internal temperature and the maximum pore air humidity. These quantities capture the rapid thermal and gas-phase response of the benchmark more clearly than grain moisture content over the first 28.3 h.

Both indicators are internal-field quantities, so their values and locations depend on the assumed geometry, boundary conditions and source parameters. The present calculations should therefore be used as a computational benchmark for method development and sensor-placement studies, not as direct operational thresholds for industrial storage.

Overall, the model reproduces the expected separation between heat, gas-phase humidity and slow solid-phase moisture response in an effective porous grain medium. The results are reproducible from the accompanying code and provide a transparent basis for later calibration against laboratory or field measurements.

4. Discussion

4.1. Timescale Separation and the Gas-Phase Water Budget

The results show that temperature, grain moisture and pore air humidity evolve on markedly different timescales, although they are fully coupled. Temperature and W respond within hours, whereas M changes by less than 4×10^{-4} percentage points over 28.3 h. This contrast is not a numerical artifact: the water budget closes to machine precision (Figure 4b), and the contrast follows from the phase capacities, about 1.7×10^3 times more water-holding mass in the solid than in the pore air, together with the small grain-moisture diffusivity. The same multi-timescale behavior, with fast pore air adjustment, slower thermal evolution and slowest solid-phase moisture change, has been inferred from instrumented columns and bins [14,25,30] and is consistent with three-dimensional silo simulations in which the core moisture remained close to its initial value of about 14% while temperature and relative humidity varied substantially [31,32]. Pore air humidity is therefore a more sensitive short-time indicator of internal biological activity than bulk grain moisture. This should not be read as evidence that grain moisture is unimportant over longer storage periods, when slow redistribution and condensation near cool walls and the roof become decisive [32].

The water-activity-based closure separates solid moisture from pore air humidity and avoids comparing variables of different physical meaning. Because W relaxes to the local interfacial equilibrium within a few relaxation times $\tau_v \approx 5.6$ h, the humidity maximum is collocated with the thermal maximum, and W_{max} depends more on the quantities that control W_i (temperature, the isotherm and its temperature correction) than on the effective vapor diffusivity: even a 335-fold increase of D_{W0} lowers W_{max} by only 2.30 g kg^{-1} and does not move it (Table 4). Natural convection weakens this collocation: with Darcy airflow, the humidity maximum moves to the upper bed while the thermal maximum stays at the bottom center (Section 3.12).

4.2. Location and Magnitude of the Hot Spot: Initial Conditions and Convection

The lower-central thermal maximum is a direct consequence of volumetric heat generation, the insulated base, symmetric cooling through the lateral and upper faces and the uniform initial state. Simulations of real silos show different patterns: in unventilated

corn silos with natural convection and solar loading, heat accumulated in the upper central region and reached about 34 °C after 30 days [31]; in metal silos, corn developed a central core of about 32 °C whereas wheat retained heat in its upper region, and the grain next to the walls and roof reached 38–41 °C under solar exposure [32]; and earlier three-dimensional bin models predicted asymmetric temperature fields driven by uneven wall exposure [15]. Localized high-temperature, high-humidity regions and humidity-stratified layers have also been studied explicitly in rice and paddy bulks [8,9]. The present benchmark, which omits buoyancy and asymmetric forcing, should therefore not be expected to reproduce the upper-core position typical of convective silos.

The non-uniform initial-condition tests (Section 3.11) show how strongly the uniform-field assumption conditions the result. An off-axis warm pocket relocates the hot spot to the pocket and raises its peak temperature by 1.40 °C (2.61 °C if the pocket is also 1 percentage point wetter), and a ±2 K vertical stratification moves the maximum upward to $z / L_z = 0.65$. Because respiration feeds back exponentially on temperature, initial non-uniformities are amplified rather than smoothed; a uniform initial field therefore tends to underestimate the local peak and to place it at the geometric thermal center of the domain. In practice, initial fields should be reconstructed from filling history and distributed temperature and humidity sensing, for example optical-fiber networks combined with data-driven field reconstruction [38], and porosity variations should be introduced as spatially varying coefficients, as in non-uniform-porosity silo models [3,5].

The Darcy-Boussinesq check (Section 3.12) separates the effect of convection on the two indicators. Over 28.3 h in a 0.5 m-deep bed, the thermal field is conduction-dominated, because heat is stored almost entirely in the grain, whereas the vapor field is advection-dominated, because the pore air carries the vapor and its effective diffusivity is small. The diffusion-only model therefore locates the thermal hot spot correctly, but overestimates the core humidity by up to about 10% and places the humidity maximum at the hot spot instead of in the upper bed, where convective moisture migration wets the surface layer [44]. In deeper beds, Ra exceeds the onset value, and convection also moves the thermal maximum upward, as in the silo simulations cited above [31,32]. Predictive storage models must therefore include the Darcy-Boussinesq airflow of Equation (7), which the supplementary code now provides as an option.

4.3. Respiration Source: Physical Basis, Nonlinearity and Uncertainty

The respiration source is the dominant short-time thermal parameter. Its baseline magnitude (≈0.16 W per kg of dry matter) is comparable to the peak heat production of 0.10–0.15 W per kg of dry matter measured for wet wheat under adiabatic conditions, and the corresponding initial heating rate of about 6.3 °C d^{-1} ($Q_{r0} / \rho c$) is of the order of the ≈5 °C d^{-1} reported for a field hot spot [13]. It is, however, far above the respiration of sound wheat at 14% d.b. [10,12]; the benchmark therefore describes a biologically active hot spot, and quantitative predictions for sound grain require a calibrated $Q_r(T,M)$ with a much smaller reference value. The pronounced asymmetry of the response to ±50% changes of Q_{r0} is explained by the analytical solution of Section 3.9: the temperature rise is a nonlinear function of t / t^*, and its elasticity with respect to Q_{r0} (1.54 at 28.3 h) increases without bound as t approaches t^*. The coefficient γ_T enters t^* in the same way. Consequently, any time-to-threshold indicator derived from the model is controlled by the uncertainty of Q_{r0} and γ_T rather than by the discretization error, which is below 0.01 °C for T_{peak}. A respiration model with a temperature optimum and thermal inhibition, calibrated against CO_2 or heat-production data, is required for long horizons [10,13].

4.4. Sorption Closure: Temperature Dependence and Hysteresis

The baseline GAB closure is single-valued and uses temperature-independent constants. First, the shift of the isotherm with temperature, which raises a_w at constant M as the grain warms [21,40], is neglected; the Clausius-Clapeyron test shows that this underestimates W_{max} by 0.56–1.75 g kg^{-1} (3.6–11.1%) for q_{st} = 3–9 kJ mol^{-1} without affecting the temperature field. Second, hysteresis is ignored. In a warming core, the grain desorbs, so that its state follows the desorption branch, on which a given M is in equilibrium with a lower a_w than on the adsorption branch [39,41]. If the isotherm parameters represent adsorption data, the model overestimates W_i and hence the vapor release and pore air humidity in the hot zone. The bounding offsets of 0.5–1.0 percentage points change W_{max} by up to 0.89 g kg^{-1} (≈6%) and the cumulative grain-to-air transfer by −21% to +19%, whereas T_{peak} is unaffected because latent heat amounts to less than 0.04% of the respiration heat over this horizon.

The effect of hysteresis would be larger under evaporation, such as in condensation cycles, for example, the diurnal cooling of walls and headspace or vapor migration from a warm core to a cold surface [32]. Between the two main branches, the grain moves along scanning curves whose slope is smaller than that of a single-valued isotherm, so that a non-hysteretic model tends to overestimate the amplitude of the water mass exchanged in each cycle and to place the onset of condensation where the main isotherm, rather than the scanning curve, predicts saturation. Over repeated cycles, these errors can accumulate and shift the predicted location and timing of wet layers. Separate adsorption and desorption branches with scanning-curve logic, together with temperature-dependent GAB constants fitted to wheat data [20,23], are therefore recommended for long-horizon simulations.

For such cycles, the single-valued closure can be replaced by a hysteretic one at modest cost. Each control volume stores the branch it currently follows and its last reversal point (M_r, $a_{w,r}$). While M decreases monotonically, a_w follows the desorption branch, and while it increases, the adsorption branch; after a reversal, a_w follows a scanning curve that starts at (M_r, $a_{w,r}$) and approaches the opposite main branch, for example by interpolating between the two branches with a weight that changes from 0 at the reversal point to 1 where the opposite branch is reached. Because the slope $\partial a_w / \partial M$ of a scanning curve is smaller than that of the main branches, the equilibrium humidity W_i responds less to small moisture changes, which limits the amplitude of condensation–evaporation exchange near cooled walls and roofs. Implementing this rule requires adsorption and desorption isotherms measured on the same grain lot [39,41] and is recommended before the model is applied to diurnal or seasonal cycles.

4.5. Explicit and Semi-Implicit Time Integration, Computational Cost and Choice of the Horizon

The forward-Euler scheme was retained because it keeps the coupling between the three fields and the source terms fully transparent and easy to reproduce. For the present coefficients, it is not stiff: the diffusion stability limit (1.85×10^3 s on the fine grid) exceeds the time steps used by a factor of about 120, and the source time scales ($\tau_v = 2.0 \times 10^4$ s; $\rho c / (Q_{r0}\gamma_T) = 1.8 \times 10^5$ s) are longer still. The reduction of Δt from 240 to 15 s keeps the diffusion number constant across grids and was not a stability requirement; with a common step, the spatial results are unchanged (Table 2). The runtime penalty of this choice is nevertheless real: with $\Delta t \propto \Delta^2$ the cost of an explicit run grows as N^5, i.e., by a factor of 32 per uniform refinement, and the fine-grid run took 35.43 s compared with 1.77 s on the base grid (Table 2).

For storage periods of weeks to months, for finer meshes that resolve wall boundary layers and for the Darcy-Boussinesq extension, unconditionally stable schemes are preferable. A semi-implicit Crank-Nicolson/Adams-Bashforth scheme [46] has therefore

been implemented (Section 2.11). It reproduces the explicit benchmark with fifteen-fold (base grid) to sixty-fold (fine grid) larger steps and is faster on the fine grid (13.8 versus 20.1 s, Section 3.13); with alternating-direction-implicit or locally one-dimensional splitting [47], as used previously by the authors for heat and moisture transfer in raw cotton [34,35], each step reduces to tridiagonal solves. When airflow is included, advection should also be treated implicitly, or the step will be limited by the advective Courant condition. The explicit scheme is retained as the reference solver because its update makes the conservation and verification checks of Section 3.9 exact and transparent. As explained in Section 2.10, the 28.3 h horizon was selected for physical reasons, not to avoid numerical divergence: both solvers remain stable beyond it, but the respiration closure then enters the runaway regime discussed in Section 4.3.

4.6. Limitations and Recommendations

The main limitations of the study and the corresponding recommendations are as follows.

(i) No experimental validation. The evidence presented is numerical verification (grid and time-step refinement, an analytical check and exact conservation). Independent multi-depth temperature, relative-humidity and CO_2 measurements in an instrumented bin are needed to calibrate Q_{r0}, γ_T and K_v and to validate the predictions, with calibration and validation datasets kept separate; for this reason, no RMSE or MAPE values are reported.

(ii) Diffusion-dominated transport. The Darcy-Boussinesq check shows that this assumption holds for heat in the present bed (Ra ≈ 1–2) but only approximately for pore air vapor, whose maximum is reduced by up to 10% and displaced upward by natural convection. Darcy airflow (Section 2.11) must be enabled for ventilated or deep beds, for long horizons and whenever humidity or moisture migration is the target quantity [3,31,32,44].

(iii) Empirical respiration closure. The exponential law has no temperature optimum, and the baseline Q_{r0} represents a biologically active hot spot; a calibrated, bounded respiration model is required for sound grain and long horizons.

(iv) Sorption closure. The isotherm is single-valued with temperature-independent constants; temperature-corrected, hysteretic isotherms should be adopted for evaporation–condensation cycles.

(v) Homogeneous medium and initial state. Uniform porosity, properties, boundary coefficients and initial fields were assumed; because initial non-uniformities change both the position and the magnitude of the hot spot, sensor-based reconstruction of initial fields and spatially varying porosity should be incorporated.

(vi) Sensitivity analysis. The Sobol' analysis (Section 3.14) covers six parameters over ±25–50% ranges at a single horizon; extending it to the diffusivities, the sorption parameters and the permeability, and to time-to-threshold outputs, is needed to rank all parameters, in particular K_v, for laboratory calibration.

(vii) Short horizon. Results are reported for 28.3 h. The semi-implicit scheme removes the explicit stability restriction, but long-horizon simulations also require a bounded respiration model, as well as the convective and hysteretic extensions discussed above.

(viii) Idealized geometry. A rectangular domain with symmetric boundary forcing was used; cylindrical silos with asymmetric solar loading and headspace dynamics are natural extensions.

Within these limitations, the benchmark provides a reproducible and verified test case for coupled heat–moisture algorithms and for evaluating numerical stability, grid dependence, source-term sensitivity and internal-state reconstruction strategies.

5. Conclusions

A three-dimensional, diffusion-dominated model of coupled heat and moisture transfer in a porous grain bed under low aeration was formulated, verified and characterized. The water-activity-based exchange closure separates solid-phase moisture, pore air vapor and interfacial transfer and conserves water and energy to machine precision. For the baseline case at 28.3 h, the peak temperature reaches 30.72 °C in the lower-central region, and the maximum pore air humidity reaches 15.79 g kg^{-1}, while grain moisture remains at 14.00% d.b.; this contrast reflects the roughly 1.7 × 10^3-fold larger water capacity of the solid phase.

Peak values are grid- and time-step-independent within 0.01%, the thermal response agrees with an analytical adiabatic-core solution, and a semi-implicit Crank-Nicolson scheme reproduces the explicit results with fifteen- to sixty-fold larger time steps. Respiration parameters dominate the temperature rise, as confirmed by Sobol' indices, whereas the interphase transfer coefficient and its interaction with respiration control pore air humidity; non-uniform initial fields relocate and intensify the hot spot. A Darcy-Boussinesq check with the measured permeability of wheat shows that the diffusion-dominated assumption holds for heat in this bed but not strictly for vapor, whose maximum is reduced by up to 10% and displaced upward by natural convection. The model is a reproducible numerical benchmark rather than an experimentally validated storage model; calibration against measurements, coupled airflow for deeper beds and longer horizons, hysteretic and temperature-dependent sorption, and sensor-based initial fields are the next steps.

Supplementary Materials: The following supporting information can be downloaded at: https://www.mdpi.com/article/10.3390/agriengineering8120508/s1, Supplementary File S1 contains the Python (version 3.12; NumPy ≥ 1.26, SciPy ≥ 1.11 and Matplotlib 3.11.2) source code used to reproduce the baseline simulation, grid and time-step refinement, analytical and balance checks, sensitivity, factorial and robustness analyses and Figures 2–4, together with a README and dependency list. The second-revision scripts model_conv.py, model_imp.py and revision_round2.py reproduce the natural-convection check, the semi-implicit time integration and the Sobol' analysis (Tables 6–8).

Author Contributions: Conceptualization, N.R., I.S. and Z.A.; methodology, N.R., I.S. and Z.A.; software, I.S. and A.I.; validation, N.R., I.S. and N.T.; formal analysis, N.R., Z.A. and Z.M.; investigation, N.T., A.I. and A.Z.; data curation, A.I. and N.T.; writing—original draft preparation, Z.A., I.S. and Z.M.; writing—review and editing, N.R., Z.A., Z.M. and A.Z.; visualization, A.I. and A.Z.; supervision, N.R. and I.S.; project administration, Z.A. All authors have read and agreed to the published version of the manuscript.

Funding: This research received no external funding.

Institutional Review Board Statement: Not applicable. This study did not involve human participants, human biological materials, personal data or animal experiments; it is a computational numerical modeling study.

Informed Consent Statement: Not applicable.

Data Availability Statement: All numerical data reported in this study are generated by the model from the parameters listed in Table 1. The source code needed to reproduce the simulations, grid and time-step refinement, analytical and balance checks, sensitivity and robustness analyses and Figures 2–4 is provided in Supplementary File S1. No external experimental dataset was used in the present study. The second-revision scripts model_conv.py, model_imp.py and revision_round2.py reproduce the natural-convection check, the semi-implicit time integration and the Sobol' analysis (Tables 6–8).

Acknowledgments: During the preparation of this manuscript, the authors used ChatGPT (GPT-5, OpenAI) for language editing and manuscript refinement. The authors reviewed and edited the output

and take full responsibility for the content of this publication. During the second revision, Claude (Opus 5.5, Anthropic) was used to assist with implementing and documenting the natural-convection, semi-implicit and global sensitivity analyses and with drafting the corresponding text; the authors checked the code, results and text and take full responsibility for them.

Conflicts of Interest: The authors declare no conflicts of interest.

Nomenclature

Symbol	Description	Unit
T	Grain-bed temperature	K or °C
M	Grain moisture content, dry basis	kg kg^{-1}
W	Pore air absolute humidity	kg kg^{-1}; g kg^{-1} in plots
Q_r	Respiration heat-generation term	W m^{-3}
Q_{r0}	Reference respiration source	W m^{-3}
S_v	Volumetric grain-air vapor-exchange term	kg m^{-3} s^{-1}
a_w	Water activity at the grain surface	–
W_i	Equilibrium interfacial absolute humidity	kg kg^{-1}
K_v	Volumetric vapor-transfer coefficient	kg m^{-3} s^{-1}
β_v	Specific volumetric vapor-transfer rate coefficient	s^{-1}
ρ	Bulk grain density	kg m^{-3}
ρ_s	Density of the solid grain phase	kg m^{-3}
ρ_a	Density of pore air	kg m^{-3}
c	Effective specific heat capacity	J kg^{-1} K^{-1}
ε	Porosity of the grain bed	–
λ_{eff}	Effective thermal conductivity	W m^{-1} K^{-1}
D_T	Effective thermal diffusivity	m^2 s^{-1}
D_{M0}	Reference grain-moisture diffusivity	m^2 s^{-1}
E_M	Moisture-diffusion activation energy	J mol^{-1}
β_M	Moisture sensitivity of D_M	(kg kg^{-1})$^{-1}$
D_W	Effective pore air humidity diffusivity	m^2 s^{-1}
h_T	Boundary heat-transfer coefficient	W m^{-2} K^{-1}
h_W	Boundary vapor-transfer velocity	m s^{-1}
γ_T	Respiration temperature sensitivity	K^{-1}
γ_M	Respiration moisture sensitivity	(kg kg^{-1})$^{-1}$
L_v	Latent heat of vaporization	J kg^{-1}
P	Atmospheric pressure	Pa
M_m, C, K	GAB sorption parameters	Variable-dependent
p_{sat}	Saturation vapor pressure of water	Pa
T_0	Initial or reference temperature	K or °C
M_0	Initial grain moisture content	kg kg^{-1}
W_0	Initial pore air absolute humidity	kg kg^{-1}
T_∞	Ambient air temperature	K or °C
W_∞	Ambient absolute humidity	kg kg^{-1}
L_x, L_y, L_z	Domain dimensions	m
Ω	Computational domain	–
θ	Temperature rise above T_0	K
t^*	Finite runaway time of the adiabatic core	s or h
τ_v	Gas-phase relaxation time, $\rho_a\varepsilon/K_v$	s
q_{st}	Net isosteric heat of sorption	J mol^{-1}
ΔM_h	Hysteresis offset of the sorption isotherm	kg kg^{-1}
n	Outward unit normal vector	–
u	Darcy (superficial) velocity of the pore air	m s^{-1}
κ	Permeability of the grain bed	m^2
μ	Dynamic viscosity of air	Pa s

https://doi.org/10.3390/agriengineering8120508

p'	Pressure deviation from the hydrostatic state	Pa
β	Thermal expansion coefficient of air	K^{-1}
c_{pa}	Specific heat capacity of air	J kg^{-1} K^{-1}
g	Gravitational acceleration	m s^{-2}
Ra	Filtration Rayleigh number, Equation (8)	–
A_Φ, b_Φ, N_Φ	Discrete linear operator, boundary vector and nonlinear terms of field Φ, Equation (9)	Variable-dependent
S_i, S_{Ti}	First-order and total Sobol' indices	–

References

1. Panigrahi, S.S.; Singh, C.B.; Fielke, J.; Zare, D. Modeling of heat and mass transfer within the grain storage ecosystem using numerical methods: A review. *Dry. Technol.* **2020**, *38*, 1677–1697. https://doi.org/10.1080/07373937.2019.1656643.
2. Hammami, F.; Ben Mabrouk, S.; Mami, A. Modelling and simulation of heat exchange and moisture content in a cereal storage silo. *Math. Comput. Model. Dyn. Syst.* **2016**, *22*, 207–220. https://doi.org/10.1080/13873954.2016.1157823.
3. Zheng, D.; Li, L.; Chen, G.; Zhou, Y.; Liu, K. Numerical Study of Low-Temperature Ventilation Drying in a Wheat Grain Silo Considering Non-Uniform Porosity Distribution. *Appl. Sci.* **2024**, *14*, 96. https://doi.org/10.3390/app14010096.
4. Li, X.; Wang, Y.; Yang, K.; Du, X. Numerical Study of Heat and Mass Transfer during Drying Process of Barley Grain Piles Based on the Pore Scale. *J. Food Process Eng.* **2023**, *46*, e14433. https://doi.org/10.1111/jfpe.14433.
5. Ge, M.; Chen, G.; Liu, W.; Liu, C. Study of Heat and Mass Transfer during Drying Process of Maize Grain Pile Based on Computed Tomography. *Biosyst. Eng.* **2024**, *248*, 82–96. https://doi.org/10.1016/j.biosystemseng.2024.10.003.
6. Liu, D.; Liu, Z.; Liu, S.; Feng, T. Coupling drying of wet and heat field of corn pile based on porous medium model. *J. Food Process Eng.* **2024**, *47*, e14645. https://doi.org/10.1111/jfpe.14645.
7. Zhang, B.; Guo, X.; Yao, Z.; Li, J.; Zhang, M.; Xu, X. Numerical simulation and energy consumption analysis of ventilation patterns in grain silo. *J. Stored Prod. Res.* **2024**, *109*, 102469. https://doi.org/10.1016/j.jspr.2024.102469.
8. Yin, Q.; Li, J.; Liu, X.; Zhang, Y.; Song, S.; Li, H. Heat and moisture transfer patterns in localized high-temperature and high-humidity regions within rice grain stacks. *Case Stud. Therm. Eng.* **2025**, *69*, 105968. https://doi.org/10.1016/j.csite.2025.105968.
9. Yin, Q.; He, Y.; Liu, S.; Liu, X.; Zhang, Y.; Song, S.; Li, H. Heat and moisture transfer dynamics in humidity-stratified paddy grain bulk under mechanical ventilation. *Results Eng.* **2025**, *27*, 106131. https://doi.org/10.1016/j.rineng.2025.106131.
10. Kibar, H. CO2 respiration rates of einkorn wheat at different temperature and moisture contents. *Turk. J. Agric. For.* **2021**, *45*, 179–190. https://doi.org/10.3906/tar-2005-38.
11. Yin, C.; Wang, Y.; Fang, Q.; Chen, X.; Yan, H.; Ma, L. Self-heating and spontaneous ignition of biomass storage piles: Towards a reliable prediction tool. *Renew. Energy* **2024**, *228*, 120683. https://doi.org/10.1016/j.renene.2024.120683.
12. Karunakaran, C.; Muir, W.E.; Jayas, D.S.; White, N.D.G.; Abramson, D. Safe storage time of high moisture wheat. *J. Stored Prod. Res.* **2001**, *37*, 303–312. https://doi.org/10.1016/S0022-474X(00)00033-3.
13. Zhang, Q.; Muir, W.E.; Sinha, R.N.; Cenkowski, S. Heat production in wet wheat under adiabatic conditions. *Can. Agric. Eng.* **1992**, *34*, 233–239.
14. Thorpe, G.R. Moisture diffusion through bulk grain. *J. Stored Prod. Res.* **1981**, *17*, 39–42. https://doi.org/10.1016/0022-474X(81)90031-X.
15. Jian, F.; Jayas, D.S.; White, N.D.G.; Alagusundaram, K. A three-dimensional, asymmetric, and transient model to predict grain temperatures in grain storage bins. *Trans. ASAE* **2005**, *48*, 263–271. https://doi.org/10.13031/2013.17927.
16. Adizova, Z.; Shadmanov, I. Mathematical modeling of heat and moisture exchange processes for grain storage. *AIP Conf. Proc.* **2024**, *3244*, 020042. https://doi.org/10.1063/5.0241493.
17. Shadmanov, I.; Adizova, Z.; Eshankulov, H. Development of mathematical models, numerical algorithms and software for monitoring and forecasting the processes of heat transfer and moisture loss during the storage of grain and cereals. *AIP Conf. Proc.* **2025**, *3268*, 020035. https://doi.org/10.1063/5.0257264.
18. Ravshanov, N.; Adizova, Z.; Murodova, G.; Turaeva, G. Development of a mathematical model for describing the spatial dynamics of temperatures and humidity levels in grain storage facilities. In *Proceedings of the Fourth International Conference on Digital Technologies, Optics, and Materials Science (DTIEE 2025), Bukhara, Uzbekistan, 20–23 May 2025*; Gibadullin, A., Eshankulov, K., Eds.; SPIE: Bellingham, WA, USA, 2025; Volume 13662. https://doi.org/10.1117/12.3071762.
19. Chung, D.S.; Pfost, H.B. Adsorption and desorption of water vapor by cereal grains and their products. Part I: Heat and free energy changes of adsorption and desorption. *Trans. ASAE* **1967**, *10*, 549–555. https://doi.org/10.13031/2013.39726.

20. Sun, D.-W.; Woods, J.L. The selection of sorption isotherm equations for wheat based on the fitting of available data. *J. Stored Prod. Res.* **1994**, *30*, 27–39. https://doi.org/10.1016/0022-474X(94)90270-4.
21. Iglesias, H.A.; Chirife, J. Prediction of the effect of temperature on water sorption isotherms of food materials. *J. Food Technol.* **1976**, *11*, 109–116. https://doi.org/10.1111/j.1365-2621.1976.tb00707.x.
22. Westgate, P.; Lee, J.Y.; Ladisch, M.R. Modeling of equilibrium sorption of water vapor on starch materials. *Trans. ASAE* **1992**, *35*, 213–219. https://doi.org/10.13031/2013.28590.
23. Thorpe, G.R. The significance of the sorption isotherm on the simulated performance of grain driers. *Appl. Sci.* **2025**, *15*, 2871. https://doi.org/10.3390/app15052871.
24. Lopes, D.C.; Neto, A.J.S.; Júnior, R.V. Comparison of equilibrium models for grain aeration. *J. Stored Prod. Res.* **2015**, *60*, 11–18. https://doi.org/10.1016/j.jspr.2014.11.001.
25. Hunter, A.J. Temperature and moisture front movement in an aerated seed bulk. *J. Agric. Eng. Res.* **1988**, *40*, 113–127. https://doi.org/10.1016/0021-8634(88)90109-6.
26. de Moraes, R.S.; Coradi, P.C.; Nunes, M.T.; Leal, M.M.; Muller, E.I.; Teodoro, P.E.; Flores, E.M.M. Thick layer drying and storage of rice grain cultivars in silo-dryer-aerator: Quality evaluation at low drying temperature. *Heliyon* **2023**, *9*, e17962. https://doi.org/10.1016/j.heliyon.2023.e17962.
27. Chang, C.S.; Converse, H.H.; Steele, J.L. Modeling of temperature of grain during storage with aeration. *Trans. ASAE* **1993**, *36*, 509–519. https://doi.org/10.13031/2013.28367.
28. Wang, Y.; Duan, H.; Zhang, H.; Fang, Z. Modeling on heat and mass transfer in stored wheat during forced cooling ventilation. *J. Therm. Sci.* **2010**, *19*, 167–172. https://doi.org/10.1007/s11630-010-0167-5.
29. de Carvalho Lopes, D.; Martins, J.H.; Melo, E.C.; Monteiro, P.M.B. Aeration simulation of stored grain under variable air ambient conditions. *Postharvest Biol. Technol.* **2006**, *42*, 115–120. https://doi.org/10.1016/j.postharvbio.2006.05.007.
30. Thompson, T.L.; Peart, R.M.; Foster, G.H. Mathematical simulation of corn drying—A new model. *Trans. ASAE* **1968**, *11*, 582–586. https://doi.org/10.13031/2013.39473.
31. Molina-Herrera, F.I.; Quemada-Villagómez, L.I.; Calderón-Ramírez, M.; Martínez-González, G.M.; Jiménez-Islas, H. Modeling Temperature and Moisture Dynamics in Corn Storage Silos: A Comparative 2D and 3D Approach. *Modelling* **2025**, *6*, 7. https://doi.org/10.3390/modelling6010007.
32. Molina-Herrera, F.I.; Quemada-Villagómez, L.I.; Calderón-Ramírez, M.; Martínez-González, G.M.; Jiménez-Islas, H. Three-dimensional modeling of natural convection during postharvest storage of corn and wheat in metal silos in the Bajío region of Mexico. *Eng* **2025**, *6*, 224. https://doi.org/10.3390/eng6090224.
33. Shadmanov, I.U.; Shafiyev, T.R. Mathematical modeling of the processes of combined heat and moisture transfer during storage and drying of raw cotton. *E3S Web Conf.* **2023**, *431*, 01060. https://doi.org/10.1051/e3sconf/202343101060.
34. Ravshanov, N.; Shadmanov, I.; Kubyashev, K.; Khikmatullaev, S. Mathematical modeling and research of heat and moisture transfer processes in porous media. *E3S Web Conf.* **2021**, *264*, 01038. https://doi.org/10.1051/e3sconf/202126401038.
35. Ravshanov, N.; Shadmanov, I. Fractional modeling of coupled heat and moisture transfer with gas-pressure-driven flow in raw cotton. *Processes* **2026**, *14*, 481. https://doi.org/10.3390/pr14030481.
36. Ravshanov, N.; Shadmanov, I. Three-dimensional multiphysics mathematical modeling of heat and mass transfer in stored raw cotton considering microbiological heat generation and environmental effects. *Nat. Eng. Sci.* **2026**, *11*, 247–263. https://doi.org/10.28978/nesciences.263021.
37. Shadmanov, I.U. Simulation and experimental studies of heat and moisture transfer processes during the storage and drying of heterogeneous porous products in open areas under solar influence. In *Proceedings of the 15th International Conference on Thermal Engineering: Theory and Applications*; Toronto Metropolitan University Library: Toronto, ON, Canada, 2024; Volume 1, pp. 28–31.
38. Wang, W.; Qin, J.; Zhang, J.; Cai, J.; Wei, G.; Ren, S. Three-dimensional temperature field reconstruction and dynamic prediction of grain bulk thermal processes based on distributed optical fiber sensing and STC-GRU. *Processes* **2026**, *14*, 2270. https://doi.org/10.3390/pr14142270.
39. Chung, D.S.; Pfost, H.B. Adsorption and desorption of water vapor by cereal grains and their products. Part III: A hypothesis for explaining the hysteresis effect. *Trans. ASAE* **1967**, *10*, 556–557. https://doi.org/10.13031/2013.39728.
40. Öztekin, S.; Soysal, Y. Determination of isosteric sorption heat for some starchy grains. *Turk. J. Agric. For.* **2000**, *24*, 713–719. (In Turkish)
41. Zeymer, J.S.; Corrêa, P.C.; Oliveira, G.H.H.; Baptestini, F.M.; Campos, R.C. Mathematical modeling and hysteresis of sorption isotherms for paddy rice grains. *Eng. Agríc.* **2019**, *39*, 524–532. https://doi.org/10.1590/1809-4430-Eng.Agric.v39n4p524-532/2019.

42. Roache, P.J. Perspective: A method for uniform reporting of grid refinement studies. *J. Fluids Eng.* **1994**, *116*, 405–413. https://doi.org/10.1115/1.2910291.
43. Nield, D.A.; Bejan, A. *Convection in Porous Media*, 5th ed.; Springer: Cham, Switzerland, 2017. https://doi.org/10.1007/978-3-319-49562-0.
44. Singh, A.K.; Leonardi, E.; Thorpe, G.R. A solution procedure for the equations that govern three-dimensional free convection in bulk stored grains. *Trans. ASAE* **1993**, *36*, 1159–1173.
45. Montross, M.D.; McNeill, S.G. Permeability of corn, soybeans, and soft red and white winter wheat as affected by bulk density. *Appl. Eng. Agric.* **2005**, *21*, 479–484. https://doi.org/10.13031/2013.18444.
46. Crank, J.; Nicolson, P. A practical method for numerical evaluation of solutions of partial differential equations of the heat-conduction type. *Math. Proc. Camb. Philos. Soc.* **1947**, *43*, 50–67. https://doi.org/10.1017/S0305004100023197.
47. Peaceman, D.W.; Rachford, H.H. The numerical solution of parabolic and elliptic differential equations. *J. Soc. Ind. Appl. Math.* **1955**, *3*, 28–41. https://doi.org/10.1137/0103003.
48. Sobol', I.M. Global sensitivity indices for nonlinear mathematical models and their Monte Carlo estimates. *Math. Comput. Simul.* **2001**, *55*, 271–280. https://doi.org/10.1016/S0378-4754(00)00270-6.
49. Saltelli, A.; Ratto, M.; Andres, T.; Campolongo, F.; Cariboni, J.; Gatelli, D.; Saisana, M.; Tarantola, S. *Global Sensitivity Analysis. The Primer*; John Wiley & Sons: Chichester, UK, 2008. https://doi.org/10.1002/9780470725184.
50. Saltelli, A.; Annoni, P.; Azzini, I.; Campolongo, F.; Ratto, M.; Tarantola, S. Variance based sensitivity analysis of model output. Design and estimator for the total sensitivity index. *Comput. Phys. Commun.* **2010**, *181*, 259–270. https://doi.org/10.1016/j.cpc.2009.09.018.

Disclaimer/Publisher's Note: The statements, opinions and data contained in all publications are solely those of the individual author(s) and contributor(s) and not of MDPI and/or the editor(s). MDPI and/or the editor(s) disclaim responsibility for any injury to people or property resulting from any ideas, methods, instructions or products referred to in the content.